# Heterogeneous catalytic reactions studied with transient gas supply and event-averaged ambient pressure x-ray photoelectron spectroscopy

Qianhui Liu

Supervisor: Jan Knudsen

Examiner: Carina Fasth

June 2022


LUND UNIVERSITY

LTH

FACULTY OF ENGINEERING

---

MASTER THESIS

NANOSCIENCE

LUND UNIVERSITY

# Acknowledgement

I sincerely appreciate the support from my supervisor Dr. Jan Knudsen, and am very thankful for having sufficient discussions with him about my progress and challenges during the 9 months of the thesis work. All his helps on Igor software, physical theories, and academic writing enhanced my theoretical understanding of the topic, practically skills on the software, and essential scientific writing capabilities as a potential researcher. This project would not be accomplished without the great support I received from him.

I appreciate the help from Virginia, Calley, Alexander, Esko during the beamtime in SPECIES, MAXIV laboratory, which was my first experience of beamtime. They helped me a lot on being familiar with the APXPS instrument and the working environment, and I learnt the APXPS operation and time resolved measurement from them. This helped me gain experience in APXPS testing and working in synchrotron radiation facilities. Besides, the experimental work helped me collaborate with my theoretical knowledge, and also laid foundation on my further study in this area.

I would like to thank my parents for the selfless dedication and great support during my Master study. And I would also thank my very important friend, who inspired me to strive for a better version of myself. It was my best luck to meet you in Sweden. And I always believe, du kan mer än du tror.

# Abstract

CO oxidation over Pd(100) is studied with ambient pressure x-ray photoelectron spectroscopy (APXPS). Cyclic gas composition pulsing of the $CO:O_2$ ratio, combined with a new method using software based event-averaging by image recognition over many pulses, is used to improve the signal-to-noise ratio substantially. Hereby, it becomes possible to follow the dynamics of Pd(100) restructuring between an oxidized surface and CO covered surface *in situ* while the reaction is running and with sub-second time resolution.

Even though the experiments suffered from $CO_2$ production at a platinum based heater filament the time-resolved measurements made it possible to follow the surface phase transitions and in particular distinguish when increased $CO_2$ production is caused by changes on the Pd(100) surface. By time evolution analysis of components from both gas phase and surface, it is demonstrated that the surface turns active before it becomes oxidized.

Finally, the work includes one of the first statistical analysis of multi-pulse experiments. This analysis reveals large fluctuations of the time the Pd(100) surface is CO-covered between individual experiments. However, the detailed analysis of many experiments performed at different temperatures demonstrates a clear temperature dependence of the time the Pd(100) surface is CO-covered.

**Key word:** Ambient pressure x-ray photoelectron spectroscopy, Event-averaging, Pd(100) surface structure oscillation

# Acronyms

| | |
|---|---|
| **LEEM** | Low Energy Electron Microscopy |
| **HESXRD** | High Energy Surface X-ray Diffraction |
| **STM** | Scanning Tunnelling Microscopy |
| **PLIF** | Planar Laser-Induced Fluorescence |
| **SXRD** | Surface X-ray Diffraction |
| **PM-IRAS** | Polarization Modulation Infrared Reflection Absorption Spectroscopy |
| **UHV** | Ultrahigh Vacuum System |
| **EELS** | Electron Energy Loss Spectroscopy |
| **TEM** | Transmission Electron Microscope |
| **LEED** | Low-Energy Electron Diffraction |
| **IMFP** | Inelastic Mean Free Path |
| **RIXS** | Resonant Inelastic X-ray Scattering |
| **HRCLS** | High-Resolution Core Level Spectroscopy |
| **DFT** | Density Functional Theory |
| **UPS** | Ultraviolet Photoelectron Spectroscopy |

# Table of Contents

# 1. Introduction

It is of vital importance to have a clear understanding of the structure of a catalyst surface when it is active for a heterogeneous catalytic reaction. However, during the catalytic reaction, the catalyst surface structure often is dynamic and as it rapidly responds to variations of the reaction conditions such as the local gas composition or temperature. Therefore, investigations of catalyst structure changes induced by changing gas compositions is critical for understanding the structure-function relationship of the catalyst surface.

The time scale of catalytic processes varies from femto-second to days[1] (Figure 1). For my work, surface restructuring on a catalyst surface is of interest. Referring to Figure 1 the time scale of restructuring is on the millisecond to second time scale. To follow the structure-function relationship we therefore need instruments not only probing the surface structure changes and the gas phase simultaneously, but we also need to have video rate time resolution.

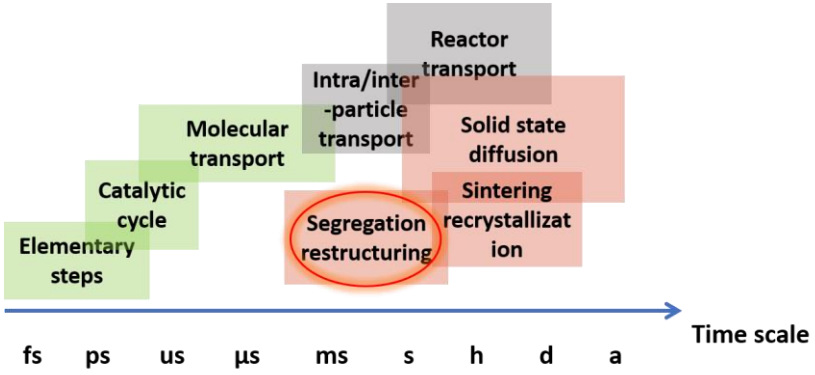


*Figure 1 Time scale of catalytic processes.*

A large number of techniques can be used for probing surface structures of catalyst surfaces *in situ*[2-5]. Figure 2 shows examples of data from different techniques. For example, imaging instruments such as scanning tunnelling microscopy (STM)[6], and low energy electron microscopy (LEEM), can image surfaces structure with atomic resolution. However, they give no information about local gas composition and have low chemical sensitivity. Miller *et al.* recently introduced an *in situ* approach for investigation of surface dynamics of a ruthenium catalyst during CO oxidation[7]. In their work, an environmental transmission electron microscope (TEM) was used to observe the surface structure with atomic resolution and electron energy loss spectroscopy (EELS) and mass spectrometry were combined with this to give an quantitative analysis of the local gas composition. This operando approach enables the detection of surface structure changes with atomic resolution and the combination with EELS gives gas composition sensitivity. However, this study suffered from low chemical sensitivity like most imaging technics. It is simply no possible to distinguish different chemical states of surface elements. In addition, TEM imaging put limits on catalyst temperature.

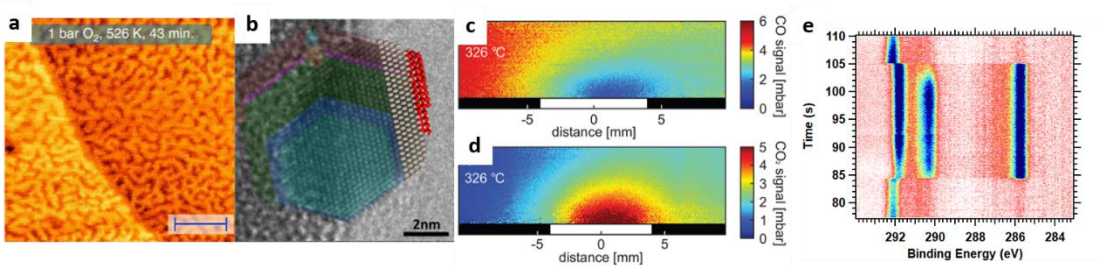


*Figure 2 Catalyst surface structure probing with different instruments and methods. a) STM image showing the Pt surface oxide under 1 bar $O_2$ at 531 K[8]. b) Atomic resolution imaging showing the Ru Wulff shape, and the oxide layer by environmental TEM of simulated model, under a gas composition of 2:1 of CO to $O_2$ ratio, at 215 °C[7]. c), d) PLIF images of the CO and $CO_2$ above the Pd(100) surface at 318 °C with gas mixture of CO, $O_2$, and Ar[9], and e) Time-resolved APXPS C 1s spectra under 280 °C with oscillating gas pulses of CO and $O_2$ rich composition.*

X-ray photoelectron spectroscopy is an efficient surface characterization method, which detects the photoelectrons from the surface of sample. It has an excellent surface sensitivity and probes both the surface composition and its chemistry[10]. Time-resolved Ambient pressure x-ray photoelectron spectroscopy (APXPS) enables the probing of the gas phase in the near vicinity of a surface, and it is widely used in surface dynamic study under variety of temperatures or pressures[11].

However, the low amounts of emitted electrons collected by the analyser in XPS and in particular in APXPS experiments leads to long acquisition times typical at the order of many seconds to minutes. This limits the application of APXPS for measuring fast processes, such as phase transitions. In additions, due to the scattering of photoelectrons in the gas phase, APXPS spectra often have a low signal-to-noise ratio, which makes detailed spectral decomposition challenging. Therefore, it is critical to develop new methodologies that can overcome the current limitations of APXPS for studying rapid phase changes.

Recently, the group where I did my master project reported a new methodology for event-averaging spectra acquired over many surface structure oscillations[12]. Using cyclic gas composition being CO and $O_2$ rich, respectively, a Pd(100) surface was oscillated between oxidized and CO covered surface structure. The concept of event-averaging, which will be explained in more detail below, is to find the same event during the repeating pulsing and give the averaged results in order to increase the signal-to-noise ratio of the spectra dramatically.

CO oxidation over a Pd(100) surface was chosen as a model for my study as well. *In situ* studies of CO oxidation over Pd(100) surface has been studied extensively with many different techniques such as low-energy electron diffraction (LEED)[13], STM[14], High Energy Surface X-ray Diffraction (HESXRD)[9], and planar laser-induced fluorescence[9, 15] (PLIF, Figure 2c), etc. During the CO oxidation reaction on Pd(100), the surface oxide, bulk oxide and chemisorbed oxygen can all be formed[12].

Previous studies found that the oxide formed on the surface significantly increase the reactivity of the surface as increased $CO_2$ production was observed when the Pd surface oxide was present[11, 16-24]. Based on this observation, studies suggested that the CO oxidation reaction is initialized by the oxidation of Pd surface which activates the surface. A CO from the gas phase interacts with the surface oxide to produce a $CO_2$, and a O vacancy on Pd, and oxygen will replenish the vacancy on the surface and the catalytic cycle can then continue. This reaction mechanism is often referred to as a Mars-van Krevelen reaction

mechanism[16].

Hendriksen et al.[25] studied CO oxidation over Pd(100) using surface x-ray diffraction (SXRD). In their experiments spontaneous oscillations of the $CO_2$ production were observed even though constant gas flows of CO, $O_2$, and Ar with high content of oxygen were injected into their reactor. The surface was observed to oscillate between oxidized surface at low CO particle pressure and metal phase covered by CO and O at high partial pressure of CO. By analysing the SXRD data they attributed the high reaction rate of the oxide surface and low reaction rate of metal surface to the higher and lower step density (roughness), respectively (Figure 3a).

Although this work did not present the experiment under CO rich gas composition, it introduced a very interesting result. Under highly $O_2$ rich condition the surface is still able to transit from oxide to metal surface, as CO molecules bind stronger to the rough Pd(001) surface O atoms. When the oxide surface gets rough, it leads to dislocations in the oxide, CO get adsorbed on the exposed metal area and further stabilize the metal surface, leading to the oxide-to-metal transition. Once CO is adsorbed on the metallic surface, the reaction follows a so-called Langmuir–Hinshelwood reaction mechanism, in which both CO and O atom adsorbed on the surface react with each other.

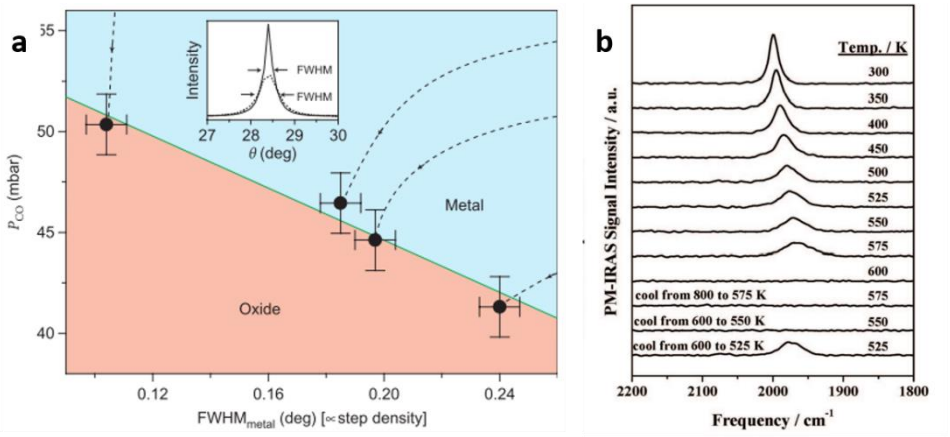


*Figure 3: a) The SXRD measurement on Pd(001) surface conducted under 460 K with a $CO/O_2$ mixture, the partial pressure of the $O_2$ is 0.48 bar. The partial pressure of CO was plotted with respect to the FWHM of the surface with is inversely proportional to the surface roughness[25]. b) PM-IRAS spectra of CO on the surface under different sample temperature[26].*

There were also studies support that the chemisorbed oxygen on the surface is more active than the oxide[18]. An early study from Gao et al.[26] suggested a different explanation. They studied the CO oxidation on the Pd and Pt surface under low pressure and near atmospheric pressure with polarization modulation infrared reflection absorption spectroscopy (PM-IRAS, Figure 3b). By measuring the gas phase pressure and the reaction temperature with respect to reaction time, they concluded that under high pressure, adsorbed CO or oxygen on the metallic surface are active with lower and higher reaction rate, respectively. However, an oxidized surface will reduce the reactivity of the catalyst surface.

In this thesis project, I will introduce event-averaging of APXPS data acquired in cyclic gas pulsing composition. The gas pulsing will make the Pd(100) surface oscillate between an CO covered surface and the surface oxide covered surface.

The Pd surface structure oscillations were then followed with time-resolved APXPS. Using event-averaging and spectral decomposition I will demonstrate how the chemical changes of the surface can be followed in the time-resolved fashion. By plotting the components peak intensity as function of time from both surface and gas phase spectra, we are able to get a full picture of the local gas composition and surface structure variation during the reaction, and especially during the phase transition. We thereby demonstrate that the surface turns to active before it is fully oxidized and even with the retention of CO on the surface. Furthermore, the CO component from gas phase measurement was analysed by integrating the signal along the time to observe a plateau of the signal several seconds after the pulsing shifts. The length of the plateau shows an obvious dependence on the operation temperature in the range from 230 to 250 °C.

# 2. Instrumentation

## 2.1. Ultrahigh vacuum system

Before the experiment, the sample surface needs to be cleaned to avoid contamination on the sample surface. Based on the kinetic theory of gas, the flux I of gas molecules impinging on the surface is given by:

$$I = \frac{p}{\sqrt{2\pi m k_B T}}$$

*Eq. 1*

Where p is the pressure, m refers to the mass of the molecules, $k_B$ is the Boltzmann's constant, and T is the temperature. The time needed to form a monolayer on the surface is then:

$$\tau = \frac{n_0}{I} = \frac{n_0\sqrt{2\pi m k_B T}}{p}$$

*Eq. 2*

Where $n_0$ is the number of atoms per monolayer. This means, under the same temperature, for example, by improving the vacuum level from $10^{-7}\ mbar$ to $10^{-9}\ mbar$, the contamination concentration decreases to 1%. Therefore, it is essential to keep a very low pressure in the cell to keep the surface clean.

Ultrahigh vacuum system (lower than $10^{-9}\ mbar$) is loaded to clean the sample surface. In my experiment, the $Ar^+$ sputtering with $1.45 \times 10^{-5}\ mbar$, 1 kV, followed by annealing the sample to 700 ℃ was used to clean the sample.

## 2.2. X ray photoelectron spectroscopy

When x-rays with sufficient energy are incident on the sample surface, electrons from core levels are emitted. These electrons produced from the photo emission process are called photoelectrons. In photoelectron spectroscopy the photoelectrons from the x-ray induced photo emission are detected. These give information of the chemical composition of the sample and the chemical state of the different elements, thus enabling the surface structure analysis.

In order to escape from the sample the kinetic energy ($E_k$) of the photoelectron needs to be larger than the sample workfunction ($\phi$). The kinetic energy of the photoelectrons is given by:

$$E_k = h\nu - E_B - \phi$$

*Eq. 3*

Where $h\nu$ is the photon energy, and $E_B$ is the binding energy. On the way a photoelectron coming out

from the sample, it risks colliding with other electrons and/or sample nuclei. Inelastic scattering with sample electrons may causes the photoelectron losing energy, which will not be detected by our energy analyzer. The average distance electrons travel in the sample before loosing energy is called inelastic mean free path (IMFP). The IMFP is dependent on the sample material lattice structure. The IMFP of electrons with energy of 100 eV in Pt sample is around 4.15 Å[27] making XPS very surface sensitive.

## 2.3. Synchrotron light

The x-ray source in my experiments was synchrotron light from the SPECIES beamline at the MAX IV laboratory, Lund. SPECIES is a soft x-ray beamline installed on the 1.5 GeV electron storage ring. It produces x-rays with an energy in the range with from 27 eV[28] to around 1500 eV, which allows valence band study, and is suitable for low Z element core level electrons.

The production of the synchrotron light consists of several steps, 1) electrons are produced from a heated thermionic cathode or a photocathode hit by a light pulse, 2) the emitted electrons entered the accelerator, in which oscillated energy field generated by RF voltage is applied to accelerated the electrons to a high energy, 3) the high energy electrons were introduced to storage ring. Under a magnetic field, the trace of electrons will be bent, through which the synchrotron radiation was produced. Based on this mechanism, several types of insertion devices including bending magnets, undulator, and wiggler are installed in the storage ring from which synchrotron light are produced through bending and dedicated to beamline. Figure 4a shows the schematic illustration of bending magnets, undulator and wiggler.

The bending magnets bends the passing electrons and synchrotron radiation is produced. The emitted synchrotron light has a range of wavelength, and the critical wavelength is given by:

$$\lambda_c = \frac{4\pi R}{3\gamma^3}\ [m]$$

*Eq. 4*

It gives a value of radiation energy that half of the photon has the energy above, half below. The undulator and wiggler are installed in the straight sections of the storage ring. They both consist of group of magnets pairs that are glued together, thus bending the light trajectory with formed magnetic field. The difference between undulator and wiggler is that undulator consists of many weaker magnets compared to wiggler, producing long signal pulse with very short range of wavelength. The light flux are interference peaks. The resonant wavelength is given by:

$$\lambda_{light} = \frac{\lambda_{undulator}}{2\gamma^2}(1 + \frac{K^2}{2})$$

*Eq. 5*

Where $\lambda_{undulator}$ is the period length for magnets, and K is the undulator parameter, given by:

$$K = \frac{eB_0\lambda_u}{2\pi m_e c}$$

*Eq. 6*

An APPLE-II type undulator is used in SPECIES beamline generating horizontally polarised light (Figure 4b). It has 41.5 periods, with one period length of 61 mm[28]. By shift the magnets pairs by certain rows in parallel mode, the x-rays are able to be polarised horizontally, vertically, or circularly.

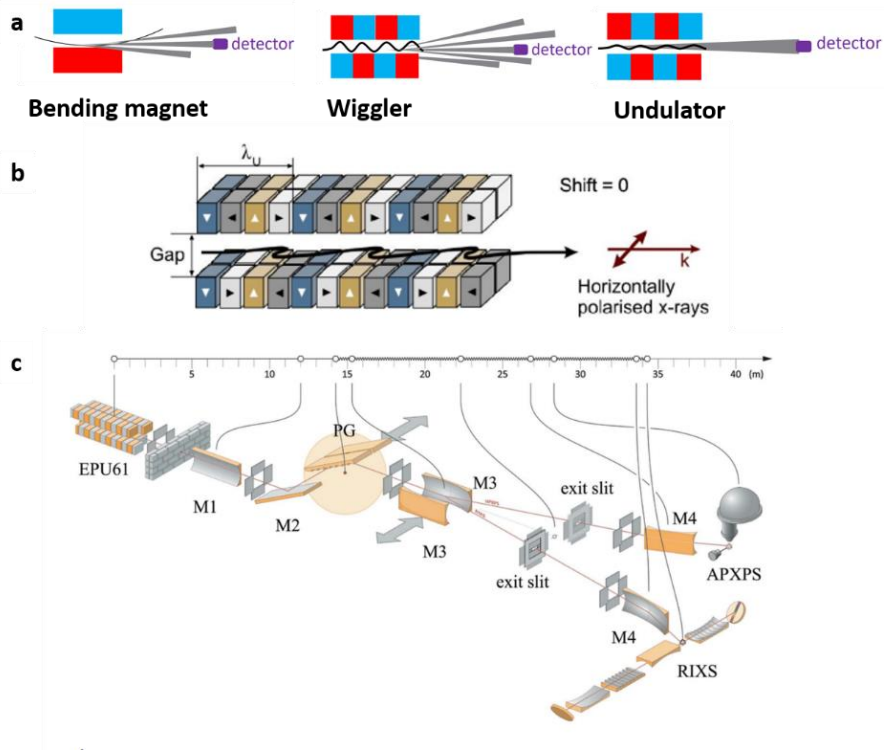


*Figure 4 Schematic graphic of a) bending magnets, undulator and wiggler, b) an APPLE-II type undulator with a horizontal polarization[29], and c) the SPECIES beamline[28].*

The produced x-rays are introduced to the beamline. The SPECIES beamline layout is illustrated in the Figure 4c[28], The x-ray coming out from the undulator (EPU61) passes the monochromator, and are then collimated vertically by a cylindrical mirror M1, focused by toroidal mirror M3, and split into two branches dedicated to resonant inelastic X-ray scattering (RIXS) and APXPS, respectively, after entering two exit slits and be refocused by two mirror M4.

## 2.4. Swept and fixed mode

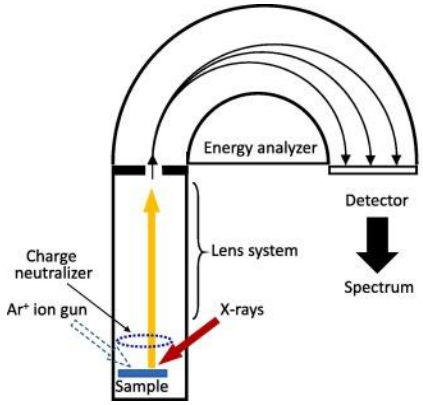


*Figure 5 Schemactic graphic of hemispherical analyzer*[30].

In my experiments the electrons were captured by a so-called electron analyser, which can be divided into two parts: A lens element, where electrons are slowed down to a certain energy, named the pass energy, and a hemispherical analyser, which only allows electrons with a kinetic energy close to the pass energy to reach the detector (see Figure 5). In the hemispherical analyser, the electrons are bent by an electrostatic field. Under a constant force, the electrons with different kinetic energy bend with different radius. Therefore, electrons with a too high or too low kinetic energy will hit the side wall of hemispherical analyser. Finally, the 2D detector collect the electrons having an energy within a small energy interval.

The analyser can be operated in so-called fixed and swept mode. In the fixed mode, the spectrum is recorded using the small energy window measured by the detector. This energy window is around 10% of the pass energy. The limited energy range makes it impossible to record the spectra of elements with large binding energy differences in each spectrum in fixed mode. In this fixed mode the time-resolution, defined by the time per xp-spectrum, is equal to the repetition rate of the detector. On the other hand, considering the local differences in the sensitivity of each detector channel, the intensity is measured with different efficiency for different kinetic energy channel. Thus the intensity measured in each channel is not strictly proportional to the intensity of electrons proportional to the amount of the corresponding chemical species on the surface. Therefore, further intensity calibration is needed.

In swept mode each kinetic energy is measured with all channels of the detector. This is achieved by scanning the so-called retarding voltage that is used to reduce the kinetic energy of the electrons before they reach the hemisphere. Hereby each photoelectron peak is swept through the energy interval of the detector. The spectrum is formed by integrating all the signals with every kinetic energy from all the channels. In this way, it reduces the error from the slight different sensitivity of the different channels of the detector. However, it takes significantly longer time to collect the data.

Hence, to obtain a high time-resolution I acquired most of my XPS measurements in fixed mode. Before starting to oscillate the gas composition, sweep mode and fixed mode spectra were acquired in a constant gas flow with intensity of $I_{sweept}$, $I_{snap}$, respectively. As is shown in Figure 6, the intensity of the spectrum acquired in fixed mode is slightly different from the spectrum acquired in swept mode. It is seen that fixed mode spectrum gives higher signal intensity in the middle of the energy window compared with the edge on both sides. The intensity of time resolved XP spectra with fixed mode can thus be calibrated ($I_{cali}$) by:

$$I_{cali} = I_0 \frac{I_{swept}}{I_{fixed}}$$

*Eq. 7*

Here $I_0$ is the intensity of the given spectrum with fixed mode, and $I_{cali}$ is the signal intensity after calibration. The intensity calibration was essential for surface measurement, while for the gas phase XPS measurement, the noise decreases significantly due to longer inelastic mean free path. Therefore, the fixed mode data was used for analysis of gas phase spectra without further calibration.

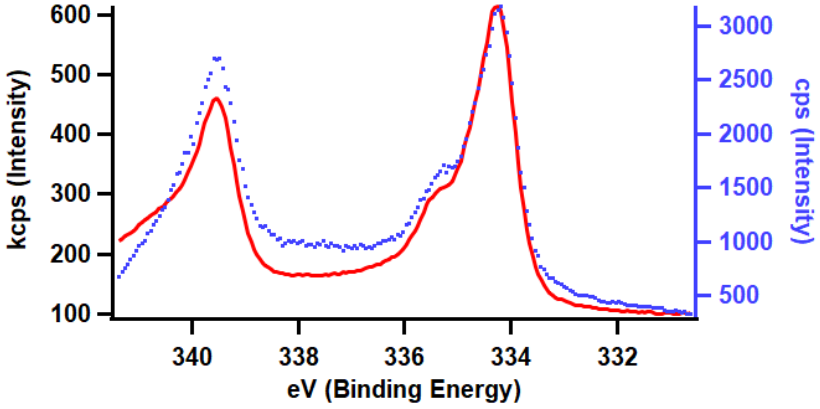


*Figure 6 Pd 3d spectra under fixed mode (blue dot) and sweep mode (red line).*

## 2.5. Gas phase and surface measurements

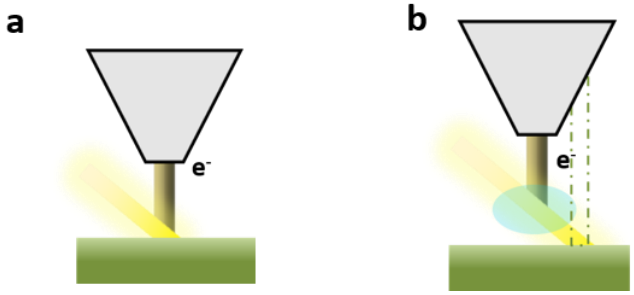


*Figure 7 a) surface measurement and b) gas phase measurement.*

The surface atom and molecules analysis is measured by positioning the sample at the normal measurement position. The incident x-ray excites the electrons from core levels, and the photoelectrons are collected by the analyzer (see Figure 7a). When we retract the sample, as is shown in Figure 7b, the emitted photoelectrons from the surface cannot reach the cone. Instead only the photoelectrons from gas phase molecules are collected. Thereby, we enable the detection of the pure gas phase signals.

# 3. Methods

## 3.1. Fermi edge calibration

The zero point of the binding energy in a XP spectrum is normally calibrated to the fermi energy[31]. In my experiments the fermi edge was measured with the same photon energy and directly after the core level spectrum which needed to be calibrated. Each fermi edge was fitted with a step function. Then the spectrum of interest was calibrated by offsetting it by offset measured for the fermi edge. Figure 8a shows an example of a fermi edge spectrum. The fitted fermi edge is shown by the red line and is located at -0.68 eV.

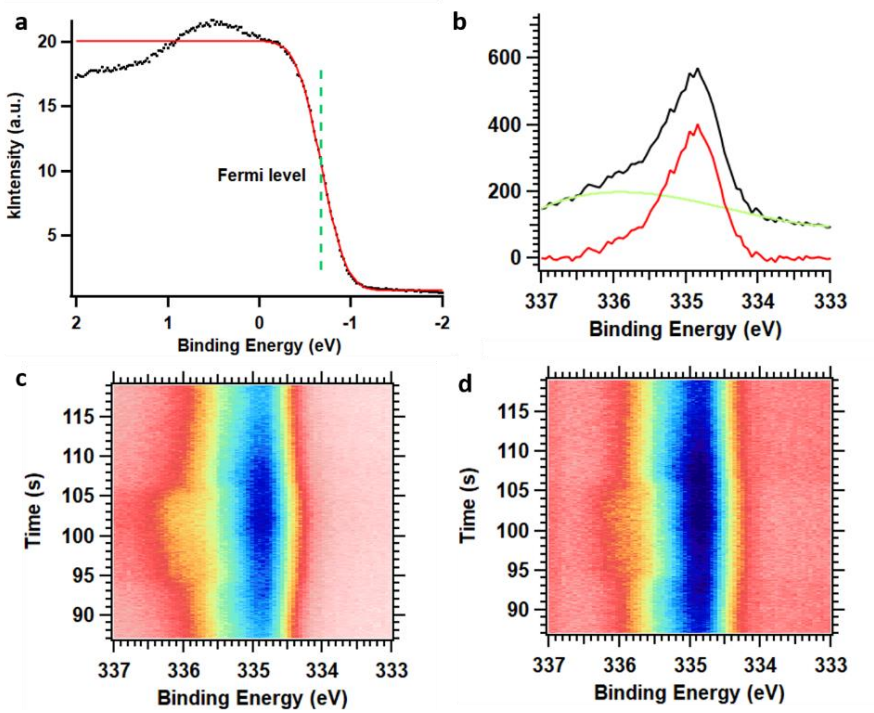


*Figure 8 a) Fermi edge of a sample (dark dots), and fitted curve (red line), of which the fermi level was measured to be -0.68 eV (green dash line). b) The Pd 3d spectrum (dark line), the background curve fitted with polynomial function (green line), and the curve after background removal (red line). Event-averaged Time-resolved Pd $3d_{5/2}$ spectra c) before and d) after background subtraction.*

## 3.2. Background subtraction

The background of a spectrum is mainly caused by the inelastic scattering of emitted photoelectrons on their way out from the solid material. The electrons that lose energy during the inelastic interaction get a lower kinetic energy and therefor ends up at higher binding energies and contribute to background signal here. Commonly used background shapes are Linear, Shirley, and Tougard[32]. In my work, polynomial functions were used for background subtraction. As discussed above, due to the detector sensitivity under the fixed mode measurement, more counts are detected in the center region of the spectrum compared

with both ends, giving the result that signal in the middle of the energy window are more intense. Therefore, polynomial functions provide better description of the background shape. Figure 8b shows a background curve fitting of Pd $3d_{5/2}$ spectrum, in which a $6^{th}$ order polynomial function is used.

To analyze the time resolved spectra which contains around 2000 spectra in one image plot in Figure 8c, it is unrealistic to subtract the background of the spectrum one by one. Instead, we consider that all the fitted background curves from one time-resolved data set should have the same shape. In more detail, a single spectrum was extracted from the event averaged image plot and the background was fitted with a 6th order polynomial function given as

$$f(x) = w[0] + w[1]x + w[2]x^2 + w[3]x^3 + w[4]x^4 + w[5]x^5 + w[6]x^6$$

*Eq. 8*

This fitted background polynomial function is then applied to all the spectra in Figure 8c with adding one more scalling constant coefficient for the intensity of the background and allowing it to freely adjust in order that it well fits every spectrum. The function is given as,

$$f(x) = (w[0] + w[1]x + w[2]x^2 + w[3]x^3 + w[4]x^4 + w[5]x^5 + w[6]x^6) \times w[7]$$

*Eq. 9*

Whereas the coefficient parameters from w[0] to w[6] are the same as the fitting function above. The background removed result is shown in Figure 8d.

## 3.3. Curve fitting

To analyse the chemical shift, how the surface composition change, how the coverage of adsorbates on the surface change, and how the gas composition above the surface change, peak decomposition of the spectra with different components representing different elements or same elements with different core level shifts are needed. The spectra are often fitted with Gaussian and Lorentzian peak components. The Gaussian peak component is given as:

$$a + H \exp\left[-\left(\frac{x - BE}{w}\right)^2\right]$$

*Eq. 10*

while the Lorentzian peak component is given as:

$$a + H \Big/ \left[1 + \left(2 \times \frac{x - BE}{w}\right)^2\right]$$

*Eq. 11*

Here, $a$ gives the vertical offset, $H$ is the intensity, $BE$ is the peak position, and $w$ refers to the width of the peak. The Gaussian and Lorentz peak components are plotted in Figure 9 with an intensity of one, a

peak center of 100 eV, and a width of 20 eV. The figure shows obvious differences between the two peak shapes. The Lorentzian peak shape is narrower around the top of the peak and has a longer extending tail, while the Gaussian peak shape is broader at the top and a smaller tail.

Theoretically, the natural line shape of XP spectra is Lorentzian, which reflects the intrinsic life-time of core hole. However, instrumental broadening leads to Gaussian broadening of the curve. The instrumental broadening can, for example, be caused by a) the energy analyser, and b) the energy distribution of the outgoing electron, etc[33].

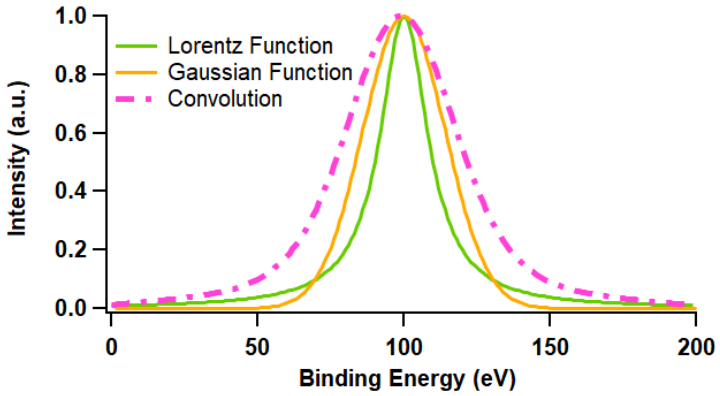


*Figure 9 Gaussian (orange) and Lorentzian function (green) with same parameter of vertical offset, intensity, and width, and the convolution of the two functions (pink).*

Therefore, simple Gaussian and Lorentzian function are not accurate to describe a spectrum. Instead, a convolution of both is needed:

$$(L * g)(BE) = \int_{-\infty}^{\infty} f(BE')g(BE - BE')d\tau$$

*Eq. 12*

The convolution modifies the shape of the function to be broader and smoother than both of the original function (Figure 9) which shows increased Gaussian character[33].

Specifically, the convolution of a Gaussian and Lorentzian function is called Voigt function which is used in the peak fitting in this work. However, it is not possible to solve the Voigt integration analytically.

Rather than performing this computational heavy convolution for every BE value, I used an approximation of Voigt function in my work named VoightIgor93. Here, it should be noticed that the peak shape in XP spectra is normally asymmetric. This is due to the secondary electrons with lower kinetic energies give contribution to the higher binding energy side of the peak.Therefore, with help of other parameters, the fitting functions are defined towards an asymmetric curve built on a Voigt profile (VoigtIgor93) as

$$w[0] + w[1] \times \text{voigtIgor}\,93(w[2] \times (x - w[3]), w[4]) \;\; (x \leq w[3])$$

and,

$$w[0] + w[1] \times \text{voigtIgor } 93\big(w[2] \times 1/\big((w[5])(x - w[3]) + 1\big) \times (x - w[3])), w[4]\big) \ (x \leq w[3])$$

Whereas, w[0] gives the vertical offset, w[1] is the intensity parameter, w[2] refers to the Gaussian component's half width at half maximum (HWHM) which is given by √ln2/HWHM, w[3] sets the peak location, w[4] is about the proportion of Lorentzian the curve is, of which w[4]=0 refers to pure Gaussian, and w[5] is the asymmetric parameter.

## 3.4. Event-averaging

The concept of event averaging is a software-based strategy aiming at increasing the signal-to-noise ratio of time resolved XP spectra, and it was first developed by Knudsen *et al.*[12].

In my experiment, time-resolved spectra were recorded under the atmosphere of cyclic gas pulsing. This leads to cyclic surface structure oscillation in response to the gas pulsing. This is in turn reflected in a periodic spectroscopic signal. Here we choose a group of signals of interest within one period as an event, which often contains signals of sharp phase transitions, or chemical shift of components. Identical events along the time can be found in one image plot of time-resolved spectra data set recorded under several tens pulses. By averaging the signal from repeated events, we thereby increase the signal-to-noise ratio of the event. To find the same events with well aligned time point is of vital importance for event averaging. Otherwise it might lead to decreased time resolution. Here, a chosen box of pixels was used as a stamp (see Figure 10a). The stamp moves along the raw data with time increment pixel by pixel to search another box with the highest similarity.

An error function calculated by comparing a potential box (containing a potential new event) with a stamp event according to:

$$\sum |p_{ij} - p_{ij+1}|^2$$

*Eq. 13*

Here, $pij$ refers to the intensities of ij pixel points of the stamp, while $p_{ij+1}$ refers to the pixel points of the box under investigation. A minimum sum of the pixels in the box reveals that a same event as the stamp was found. Thus, it can be added to the initial event with aligning to the stamp signal. As the stamp signal moves along the time increment, the error $\sum |p_{ij} - p_{ij+1}|^2$ with respect to time was plotted, of which it shows as a lowest peak point of the curve when the error reaches the minimum.

Figure 10 illustrates the event search algorithm and error function calculation. The white bar with a length of 13 pixel and width of 2 pixel is an event. The first bar is used as a stamp goes along y axis. The error function increases as the chosen box moves out from the bar (yellow dash box) and reaches the maximum when all the pixels in the box are dark (pink region). The coincident event with the stamp (green box) gives the minimum of the error.

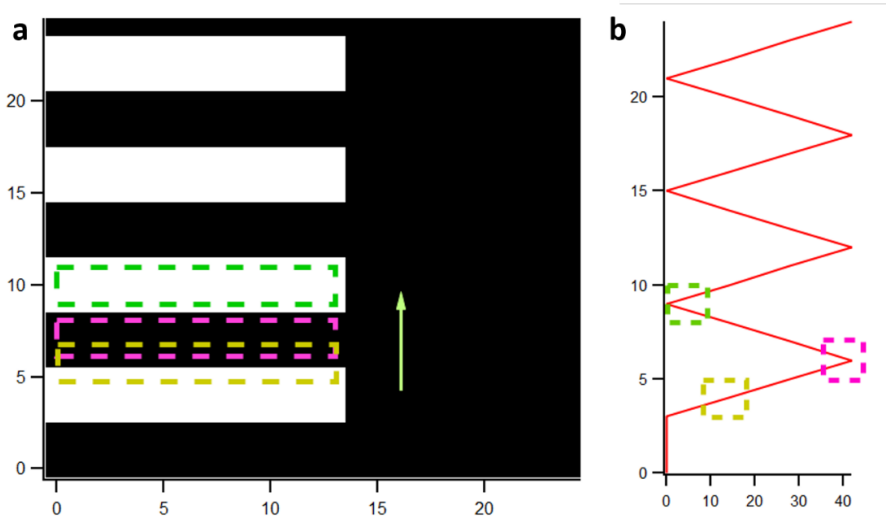


*Figure 10 a) Schematic illustration of a series of repeating events, and b) error function plot.*

When dealing with a big volume of events, it is essential and efficient to design a procedure to help find the error minimum instead of searching manually. Here, we use a polynomial function to fit the error curves, giving by

$$K_0 + K_1 x + K_2 x^2 = 0$$

*Eq. 14*

Whereas $K_2$, $K_1$ and $K_0$ are the coefficients of quadratic term, first order term and constant, respectively.

The peak minimum of the error function curve corresponds to the first order derivative

$$K_1 + 2K_2 x_{peak} = 0$$

*Eq. 15*

# 4. Results and discussion

## 4.1. Oxidized and CO covered Pd(100)

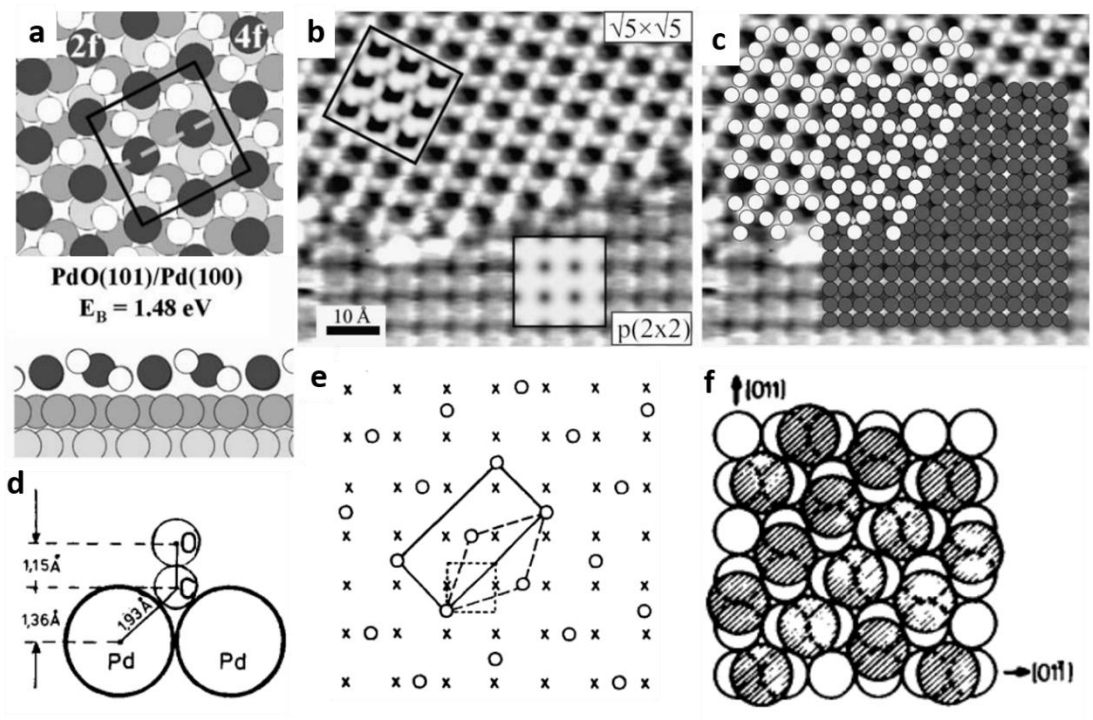


*Figure 11 a) The top-view, and side view of the structural models of Pd oxide on (100) surface reported by M. Todorova et al.[34] b), c) The experimental STM image showing the Pd(100)-$(\sqrt{5} \times \sqrt{5})R27°$-O and the $p(2 \times 2)$ phase. d) The geometry of CO sitting on the bridge site of Pd, e) the real space lattice structure, and f) the top view of the CO $c(2\sqrt{2} \times \sqrt{2})$ structure model with a coverage of $\theta = 0.5$.*

In my experiments I studied CO oxidation over Pd(100) and used this reaction to test how well the experimental setup at the SPECIES beamline can be used for event-averaged and time-resolved APXPS studies. It is known, that the Pd(100) surface structure depends on the gas stoichiometry, total pressure, and surface temperature[14]. For example, the surface can be covered by an ultrathin surface oxide or it can be covered by adsorbed CO.

The ultrathin surface oxide atop Pd(100) has previously been studied by M. Todorova *et al.* using high-resolution core level spectroscopy (HRCLS), scanning tunneling microscopy (STM), and density functional theory (DFT)[34]. This study showed that the surface oxide can be described as a $(\sqrt{5} \times \sqrt{5})$ R27°-O structure of a strained PdO(101) structure atop Pd(100) (Figure 11a-c). DFT calculations further showed that this structural model is most energetically stable compared to other reported structures. A sketch of the model is shown in Figure 11a, also illustrating that 2f (two-fold O coordinated) and 4f (four-fold O coordinated) Pd atoms exists on the surface. Additionally, bulk Pd atoms and interface atoms between the surface layer and bulk (side view of the model shown in Figure 11a) exists.

The CO covered Pd(100) surface structure is formed during the CO-rich gas pulse. The stable adsorption site of CO on the Pd(100) surface has previously been found to be the bridge site[11]. The geometrical structure model shown in Figure 11d-f was determined with LEED, Ultraviolet Photoelectron Spectroscopy (UPS) and thermal desorption measurement by Behm *et al.*[35] It shows a $c(2\sqrt{2} \times \sqrt{2})R45°$ surface structure having a CO coverage of 0.5 ML with each CO molecule bridge coordinated to two Pd atoms and with the orientation of the molecule normal to the Pd(100) surface and bond formation from the C atom to the surface.

To understand in detail how the gas composition changes the surface structure of the catalyst surface and how the varying structure in turn change the chemical activity is of vital importance. As discussed in the introduction, many previous research papers report that the Pd oxide surface has higher activity than the CO covered surface[16, 36]. From this it is natural to concluded that during the CO oxidation reaction, the Pd oxide is formed first and the surface subsequently becomes active. In contrast, the CO covered Pd(100) surface poisons the surface and suppress the reaction. In the following sections, by analyzing time-resolved spectra with event-averaging, I will discuss the catalyst surface structure and reactivity relationship, specifically which structure triggers the restructuring and how this affects the catalyst activity.

## 4.2. Steady state experiments

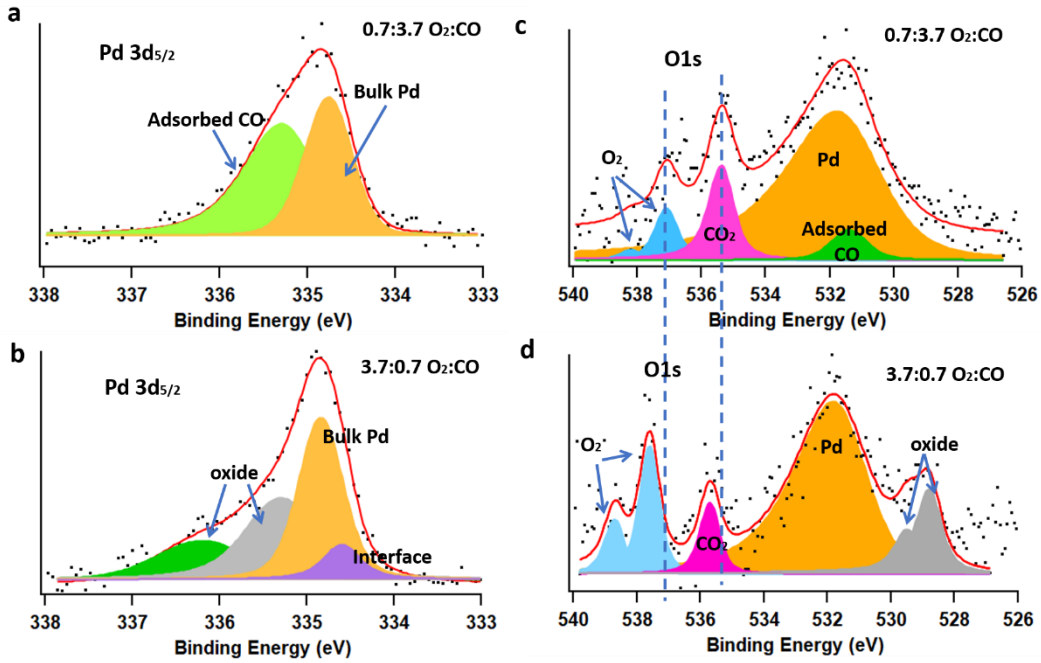


*Figure 12 Pd $3d_{5/2}$ Spectrum under the gas composition of a) 0.7:3.7 CO:$O_2$ and b) 3.7:0.7 CO:$O_2$, both the spectrum are acquired after adding up 10 spectra to reduce the noise. The O1s spectrum acquired from c) CO rich and d) O2 rich pulse same as Pd $3d_{5/2}$ measurement with binned 40 times.*

Figure 12 shows the Pd $3d_{5/2}$ and O 1s spectra of the CO covered and oxidized surface, respectively. Starting with the analysis of the Pd $3d_{5/2}$ spectra the spectrum in panel a acquired in a gas composition

of 0.7:3.7 $O_2$:CO at 280 K can be curve-fitted by two different components at 335.5 eV and 334.8 eV, respectively. The component at 335.5 eV is assigned to surface Pd atoms coordinated to adsorbed CO, while the component at 334.8 eV is assigned to bulk Pd atoms, in agreement with the reported binding energies in the literature[16].

Upon changing the gas composition to 3.7:0.7 $O_2$:CO (Figure 12b), the CO-induced component at 334.8 eV disappears and new components are observed at 336.2, 335.3, and 334.6 eV. Previous studies[16] have shown that the component at 336.2 and 335.3 eV can be assigned to the 4-fold (green peak) and 2-fold (grey peak) Pd atoms coordinated with O, respectively, and the component at the lowest binding energy is assigned to interface Pd atoms located between the oxide and the bulk atoms. Finally, the orange component is assigned to Pd bulk atoms.

Similarly, O 1s spectra acquired from the CO and $O_2$ rich gas compositions are displayed in Figure 12c and d, respectively. In a gas composition of 0.7:3.7 $O_2$:CO (Figure 12c), five components are observed. Starting with the components originating from the gas phase, the two blue components located at the highest binding energies at 538.2 and 537.1 eV, respectively, are assigned to $O_2$ in the gas phase. The component at 535.4 eV is attributed to the $CO_2$ in the gas phase produced during the reaction in agreement with the previous work[12, 16]. No CO is observed at the expected peak position of 536 eV most likely because it is shadowed by the large $O_2$ doublet. Continuing with the components originating from surface species the green component at 531.4 eV is assigned to the adsorbed CO on the surface, in agreement with the observations made in the Pd spectrum (Figure 12a). The orange component at 531.8 eV is attributed to the Pd $3p_{3/2}$, which happens to overlap with the O 1s region. The combined picture we get from the observed gas phase and surface components is that the surface is covered by adsorbed CO, while $CO_2$ still is produced. Most likely the produced $CO_2$ comes from the Pt filament as a CO covered surface normally is inactive.

When it comes to the oxygen rich environment (Figure 12d), a dramatic difference is observed from the spectrum in Figure 12c. The gas phase components from $O_2$ doublet (537.6 and 538.7 eV, respectively) and $CO_2$ (535.7 eV) are still observed but with a shifted binding energy by 0.4 eV to higher positions, compared with Figure 12c. For the components originating from the surface, the Pd $3p_{3/2}$ components (in orange) still stays with the same binding energy. No adsorbed CO component is shown on the surface, instead two grey components at 529.5 eV and 528.8 eV are observed which are assigned to the √5 oxide formation on the Pd(100) surface based on pervious studies[16]. This reveals that the surface changes from CO-covered Pd(100) metallic structure to Pd oxide structure. This also explains the binding energy shift of the gas phase components, which is caused by work function changes of the surface.

## 4.3. Time-resolved spectral analysis using event-averaging

### 4.3.1. Surface analysis

In the experiments, a Pd(100) surface was exposed in an oscillating gas mixture with a duration of 30 s for one full oscillation period. In the first 15 s the gas flow had a composition of $O_2$:CO=3.7:0.7 sccm, followed by the opposite gas composition $O_2$: CO=0.7: 3.7 for 15 s. Approximately 90 pulses are used for each experiment. The sample temperature was kept at 280 °C for all the measurements described in this section with a small variation of +6/-3 °C due to the exothermic heat from the reaction. The oscillating gas composition will make the catalyst surface structure oscillate between a CO covered surface, and a Pd oxide surface where the oxidation reaction occurs.

The C 1s spectrum was first measured in the normal sample measurement position. Here both atoms and molecules on the surface and gas phase molecules are probed. Figure 13a shows the image plot of 1880 time-resolved C 1s spectra, containing a full CO pulse in the middle, and $O_2$ rich gas compositions from t<84 s and t>105 s. The total time length of the y axis in the image plot is 33 seconds. The signal-to-noise ratio in the image plot of the time-resolved data in panel a are unfortunately not good enough to resolve and decompose the spectra. Thus, it is impossible to study when the phase transition happens, how fast the transition process is, and if any intermediate phases are formed.

To improve the signal-to-noise ratio, the image plot is event-averaged by using the region marked in black dash box as a stamp to align all the same events. Figure 13b shows the image plot after event-averaging 81 pulses. Clearly, a significant improvement of the signal-to-noise ratio is obtained compared to Figure 13a.

However, each of the 81 pulses are not necessarily fully identical. For example, the gas pulse length or the measurement frequency might change slightly during the measurement. The effect of this will be a gradually more blurry signal as one moves further and further away from the stamp where the events are aligned. This is clearly seen in panel b of Figure 13 at t = 84 to 105 s. To improve the event-averaging and account for variations of the pulses the event-averaging is performed twice using two different stamp images located at the two transition regions as shown in the dash boxes in Figure 13c. Finally, we combined the Figure 13b from t=84 to 92 s and the second event-averaged image from t=92 to 110s to form a new event-averaged image plot of the same time period. Figure 13d shows the final event-averaged image after intensity normalization, performed by diving the intensity of each spectrum with the background level at the low binding energy side, and after additional background subtraction. Three components are observed in Figure 13d, assigned to $CO_2$ and CO in the gas phase, and CO adsorbed on the surface. A shift of the apparent binding energy of the $CO_2$ component is observed at t = 84.2 s and t = 105 s and signals a work function shift of the surface.

Each spectrum from the event averaged spectra was curve-fitted. This was realized by using automatic curve-fitting procedure to determine the peak position, width, asymmetry, and Lorentzian-to-Gaussian ratio for all spectra. Only the intensity parameter was kept free when fitting individual spectra, while all other components were linked. Figure 13e and f show examples of three individual curve-fitted spectra extracted from the image plot in Figure 13d at times of 79 and 90.8 s, respectively, and highlighted with

dotted lines in panel d. In the spectrum from the $O_2$ pulse period in Figure 13e, a component at around 292.1 eV (pink peak) is clearly observed, which is assigned to the $CO_2$ in the gas phase generated from CO oxidation on the surface. Besides the $CO_2$ component a small green component at 290.4 eV is also observed in Figure 13e, assigned to the small amounts of CO in the gas phase.

Figure 13f extracted from the CO pulse period also shows the two gas phase components $CO_2$ and CO as is in the Figure 13e but with a binding energy shift by 0.2 eV to lower position. This is due to the work function of the surface changes as the surface structure changes from Pd oxide to a surface with CO adsorbed. The contribution at 285.8 eV is the evidence of the CO on the surface.

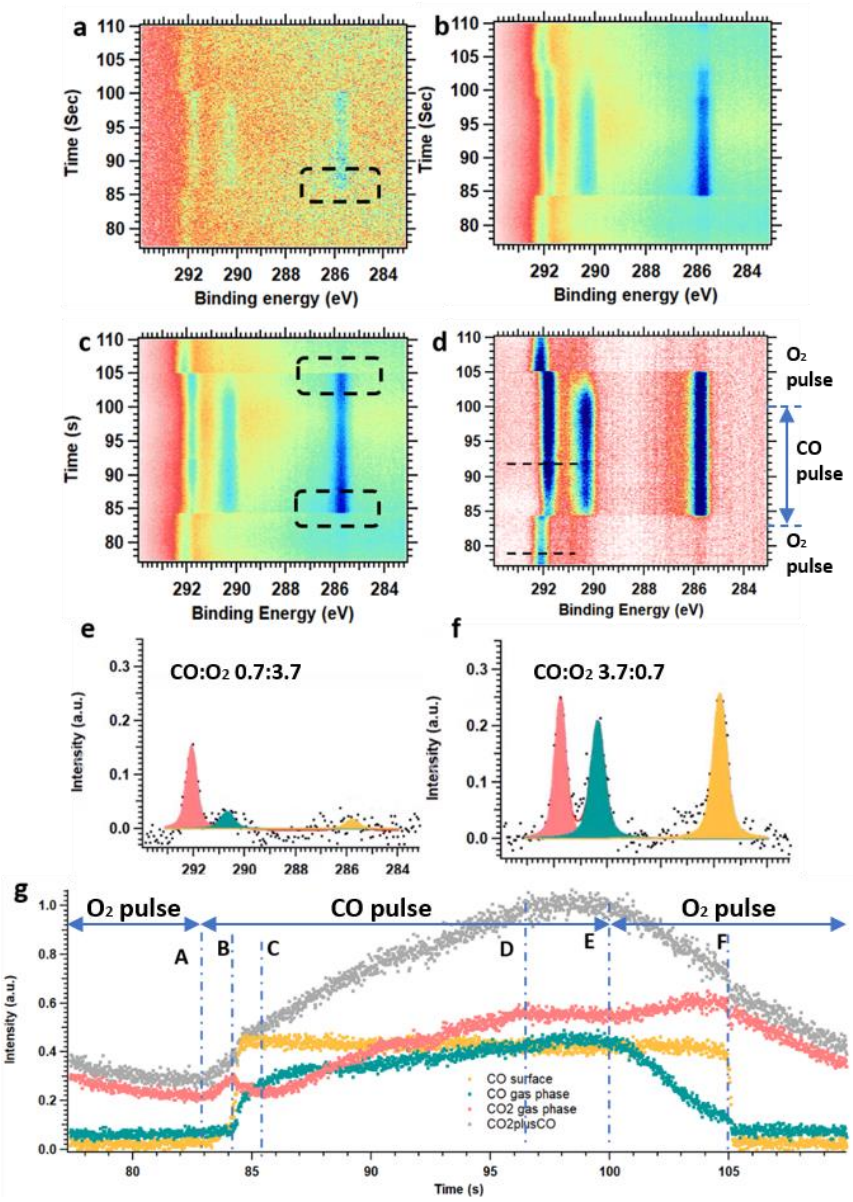


*Figure 13 a) The image plot of C 1s time-resolved spectra acquired with 57.7 Hz, showing one full CO pulse period in the middle. The C 1s image plot after event averaging with b) one stamp marked as the black dash box, and c) two stamps. And d) The event-averaged image plot of C 1s spectra after background removal, and intensity normalization. e), f) The single spectrum extracted from panel d during $O_2$ and CO pulse, and g) the intensity of components with time evolution.*

Figure 13g shows the time evolution obtained by curve-fitting all spectra in Figure 13d. At t < 83 s (before line A) before the CO rich gas composition arrives in the gas atmosphere above the sample surface CO is absent both in the gas phase and on the surface. This clearly indicates that the reaction is mass transfer limited. From line A to line B, the $CO_2$ production increases as the CO rich pulse now starts arriving. In parallel CO adsorption on the surface starts, but without any visible CO in the gas phase. The reaction must therefore still be mass transfer limited, but now small quantities of CO corresponding to 61 % of the maximum $CO_{ads}$ intensity observed in panel g is present on the surface. Later at line B both the CO on the surface and in the gas phase start to increase rapidly. This is a clear evidence that the surface becomes CO poisoned and its ability to convert CO to $CO_2$ is lost. This leads to a temporary decrease of $CO_2$ production for 2 s.

From line B to F, the adsorbed CO signal is almost constant, signaling a constant surface coverage of CO in this entire interval. Starting from line C, the $CO_2$ production is increasing, in parallel with the CO(g). We propose that the $CO_2$ in this period comes from the Pt filament. When the surface becomes inactive and fully CO covered the exothermic heat is lost. The filament needs to heat more to maintain a constant sample temperature, plus the remaining oxygen in the cell from the $O_2$ rich pulse before, we therefore observe increased $CO_2$ production from line C to D. The $CO_2$ signal reaches a plateau at around 96.5 s and last until line E suggesting that the reaction on the filament becomes mass transfer limited. We suppose this is due to the lack of oxygen in the cell since the CO signal is still increasing in the gas phase, and the Pd surface remains CO poisoned. Further, evidence for this comes from the O 1s spectra discussed in the next section.

From line E the CO signal in the gas phase starts to decrease, and the CO+$CO_2$ gas phase signal is also decreasing marking the start of the transition towards the $O_2$ rich gas atmosphere. Also starting from line E, the $CO_2$ production starts to increase. The adsorbed CO coverage is constant at the same level. Thus, the $CO_2$ production predominantly must come from the hot filament. This increased $CO_2$ production after line E we explain by the injection of $O_2$ into the cell. Consistent with an $O_2$ mass transfer limited reaction on the filament more $O_2$ injected into the cell is expected to increase the $CO_2$ production. At line F, the CO in the gas phase decreases to almost 0, in parallel with complete removal of CO on the surface. Therefore, the surface is no longer CO covered. After 105. 5 s, the surface returns to the same condition as the beginning. The decreasing $CO_2$ level in this period is due to the reaction on the filament being mass transfer limited by CO.

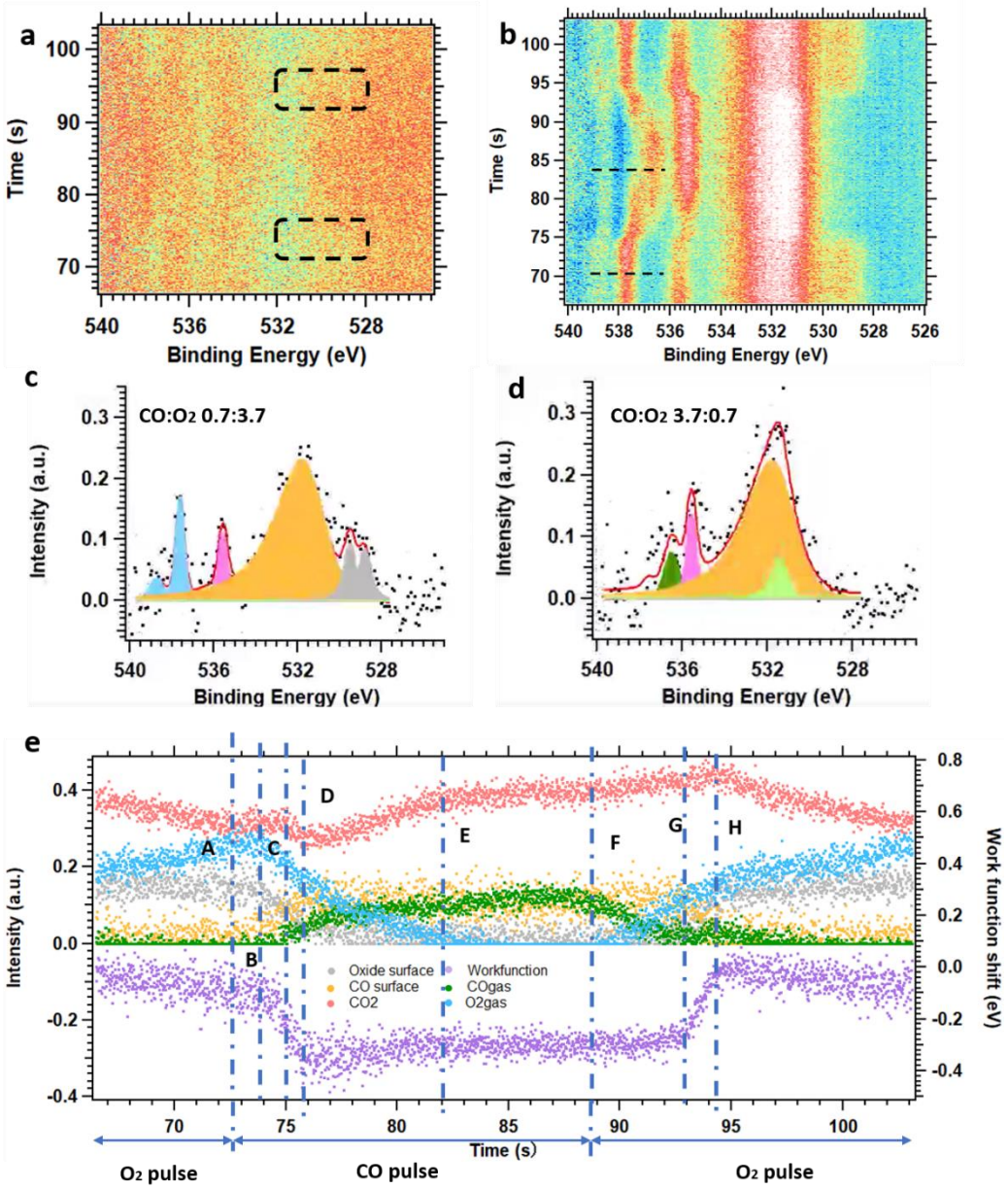


*Figure 14 The O1s surface spectra a) before, and b) after the event averaging with two stamps in marked in the dark dot rectangular square, and normalization together with background subtraction. The single O1s spectrum from the recorded movie of the fitted spectra within time resolution, of which c) is the spectrum from the $O_2$ rich pulse, and d) the spectrum from CO rich pulse. e) The intensity of CO surface component, oxide on the surface, the $CO_2$ component in the gas phase from the above fitted spectra and the workfunction shift with time resolution.*

The O1s data was acquired with a photoenergy of 800 eV and pass energy of 200 eV. Figure 14a shows the image plot of time resolved spectra acquired with a frequency of 61 Hz. After event averaging 49 pulses with two stamps marked with the dashed dark boxes (see panel a), followed by intensity normalization and background subtraction done in the same way as for C 1s, a high signal-to-noise ratio is obtained as panel b demonstrates. Each spectrum in the event-averaged image plot is curve-fitted and decomposed with Voigt functions with free adjustment for component intensities. Since the apparent binding energy of the gas phase components change during the phase transition, due to a changing work function of the sample, the positions of gas phase components are also kept as free parameters. As a result

of this the automatic curve-fitting procedure might fail to find an optimized solution, or many solutions are found which might however not physically make sense. To make the curve-fitting robust I predetermined the work function shift by curve-fitting the binding energy position of the intense $CO_2$ component and applied the binding energy shift values to other gas phase components.

Figure 14 c and d show examples of the curve-fitting of single spectra acquired in oxygen and CO rich gas composition, respectively. In panel c, the two blue components at 537.7, 538.8 eV are attributed to the $O_2$ gas phase doublet, and the pink component at 535.6 eV is assigned to $CO_2$ also in the gas phase. The orange component at 531.8 eV is due to the Pd 3p line, and the two grey components at 529.5 and 528.8 eV are evidence of surface oxide formation. The components shapes and positions are consistent with that from the steady state measurement in Figure 12 c.

The spectrum acquired in the CO rich gas composition shown in in panel d is similar to Figure 12 d at steady state. The $O_2$ gas phase doublet disappears from the gas phase and instead CO gas phase is observed as seen by the green component at 536.5 eV. The $CO_2$ component shifts to 535.4 eV due to the work function change of the sample. The Pd 3p component remains on the surface with a binding energy of 531.8 eV. The green component at 531.4 eV is assign to the adsorbed CO.

The time evolution of the intensity of the different components and the work function shift are plotted in the Figure 14 e. The $CO_2$ component in the gas phase (pink dots) shows the same trends as discussed when analysing the time-resolved C 1s data, but the noise level of O 1s data are in general higher.

From the beginning to line A (t = 72.5 s), the system is in oxygen rich gas composition. The oxide is present on the surface as evidenced by the high intensity of the oxide surface component. In this time interval $CO_2$ is produced both on the surface and by the hot filament as discussed before. The decreasing $CO_2$ production is tentatively explained by a reduced CO content in the cell while the surface reaction on the Pd(100) surface is mass transfer limited by CO, consistent with the C 1s data.

Starting from line A, $CO_2$ shows a temporary increment, which is evidence that the gas composition was shifted to CO rich pulse. The injection of CO facilitates higher $CO_2$ production but the reaction is still in the mass transfer limit. After 1.5 second (line B), the surface oxide starts reducing, in parallel with the increment of CO adsorption. In the meantime, the work function shift shows an obvious drop, which also proves a surface structure change. The replacement of oxide by CO on the surface takes 2 second which differs from the abrupt phase transition process observed in C 1s (Figure 13g). This is probably due to the high signal noise of the spectrum even after the event-averaging.

CO starts to appear in the gas phase after line C. At the same time CO adsorption is observed to increase on the surface. In the meantime a drop of the $CO_2$ production is observed, revealing a reduced reaction rate on the surface due to the CO adsorption. The re-increment of the $CO_2$ after 1 second is due to the reaction on the hot filament as we discussed in the C 1s data.

The oxide on the surface is fully removed after line D, when the CO component on the surface reaches the maximum as well as the work function shift. The increase of $CO_2$ production reaches a plateau at line E. In the C 1s discussion, we proposed this to be the mass transfer limited reaction by oxygen on the filament. Here it is proved by the absence of gas phase oxygen (blue dots) reaching 0 at line E.

At t=88.6 s (line F) the CO gas phase decreases while the surface CO remains. In the meantime the gas phase oxygen component reappears, indicating the gas composition shifts to $O_2$ rich composition. The $CO_2$ production slightly increase again from line F to G due to the injection of oxygen to the cell facilitating more $CO_2$ production the reaction on the filament as we discussed for the C 1s data.

The decrease of CO on the surface starts from line G, together with the appearance of oxide signal again. A new observation at line G is that $CO_2$ further increases with a larger slope. This was not clear in the C 1s data. We propose this might be due to the Pd surface reaction, even though it is shown not fully oxidized yet until line H. After line H, the oxide is fully developed, and the reason that $CO_2$ product decreases is due to mass transfer limited by CO as discussed for the initial time region of the graph.

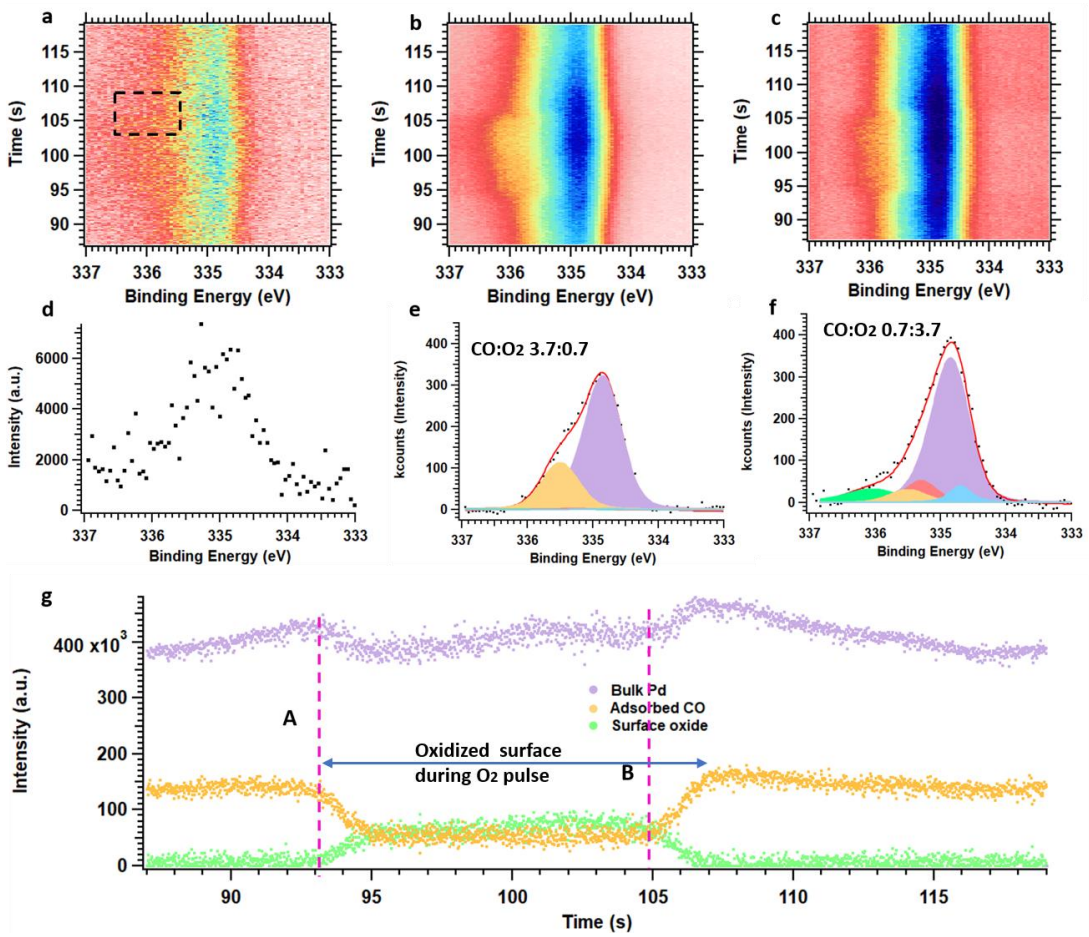


*Figure 15 Image plot of time resolved Pd 3d spectra acquired under a photon energy of 500 eV a) before, b) after event-averaging of 81 pulses, and c) after background removal. d) Single spectrum recorded from time-resolved spectra in panel a. Single spectrum extracted from panel c with curved fitted and decomposed, originating from e) CO rich pulse environment and oxygen rich environment. And g) the intensity variation of Pd components with time evolution recorded from panel c.*

By changing the photon energy to 500 eV with a pass energy of 100 eV, the Pd 3d data are acquired. Figure 15a shows an image plot of 1894 time-resolved Pd 3d spectra measured with a frequency of 59 Hz, containing a full oxygen rich pulse in the center. Similar to the C 1s time resolved spectra, the signal-to-noise ratio is too low to resolve or decompose the components in the individual spectra as Figure 15d

demonstrates. Figure 15b and c show image plots obtained by event-averaging 81 pulses using the stamp marked with the dark dashed box in Figure 15a before and after background removal, respectively. Clearly comparison of panel a and c of Figure 15 demonstrates that the signal-to-noise ratio is highly improved by event averaging. However, the transition is more difficult to resolve in the Pd 3d data than in the C 1s and O 1s image plots due to the high background and many components in the same binding energy region.

All spectra of Figure 15c are decomposed by the following Voigt components: Pd coordinated with CO, bulk Pd, Pd coordinated with O, and interface Pd. Before curve-fitting all parameters of this function (binding energy, width parameter, and Lorentzian ratio) were determined by fitting two spectra acquired in the CO rich and $O_2$ rich gas composition, respectively. Subsequently, all other spectra were fitted and only the intensity were now allowed to vary.

Examples, of curve-fitted spectra extracted from the image plot of panel c in the CO rich and oxygen rich atmosphere, respectively, are shown in panel e and f. Two components are seen in panel e, of which the yellow component at 335.5 eV corresponds to surface Pd coordinated with CO, and the purple peak at 334.8 eV is attributed to the Pd bulk atoms, which aligns well with Figure 12a. In the $O_2$ rich gas composition (panel f), five components are observed. The green and red peak at 336.1 and 335.3 eV, respectively, are assigned to the 4-fold (green peak) and 2-fold (red peak) Pd atoms coordinated with O, respectively. The blue component at the 334.7 eV is assigned to the Pd interface atoms and the purple component from the Pd bulk atoms remains.

Except for the components discussed above, the automating fitting procedure detects a small amount of the component signaling CO coordinated Pd component (yellow peak) also. This might be due to a not well-defined automatic curve fitting since there are other components such as oxide and Pd bulk are located closely. Therefore, we cannot yet draw the conclusion that the CO still remains during the entire oxygen rich pulse.

Panel g shows the time evolution of Pd 3d components obtained by curve-fitting all the spectra from panel c. From the beginning to the line A at t=93 s, the sample is in the CO rich gas composition. The presence of the CO coordinated Pd component shown as yellow dots is clear evidence that the surface initially is covered by CO. Consistently, the surface oxide signal shown in green is zero. Starting from line A, the gas composition turns oxygen rich and the intensity of CO coordinated Pd component decreases. The reason that the CO component does not disappear completely is most likely due to insufficient resolution and signal-to-noise level in the single spectra. The surface oxide component increases to a stable value within 2 s interval and maintains then an almost constant intensity during the oxygen rich gas composition. The 2 s transition time to reach the stable value is inconsistent with the abrupt shifts observed in C 1s data discussed above. We suggest that the longer transition time is caused by the limitations of the precision of the event-averaging of the Pd 3d spectra. At line B the gas composition changes back to CO pulse period, causing a reversed transition of the component intensities. Again a 2 s transition time is observed consistent with explaining this by limitations of the event averaging method.

## 4.3.2. Gas phase analysis

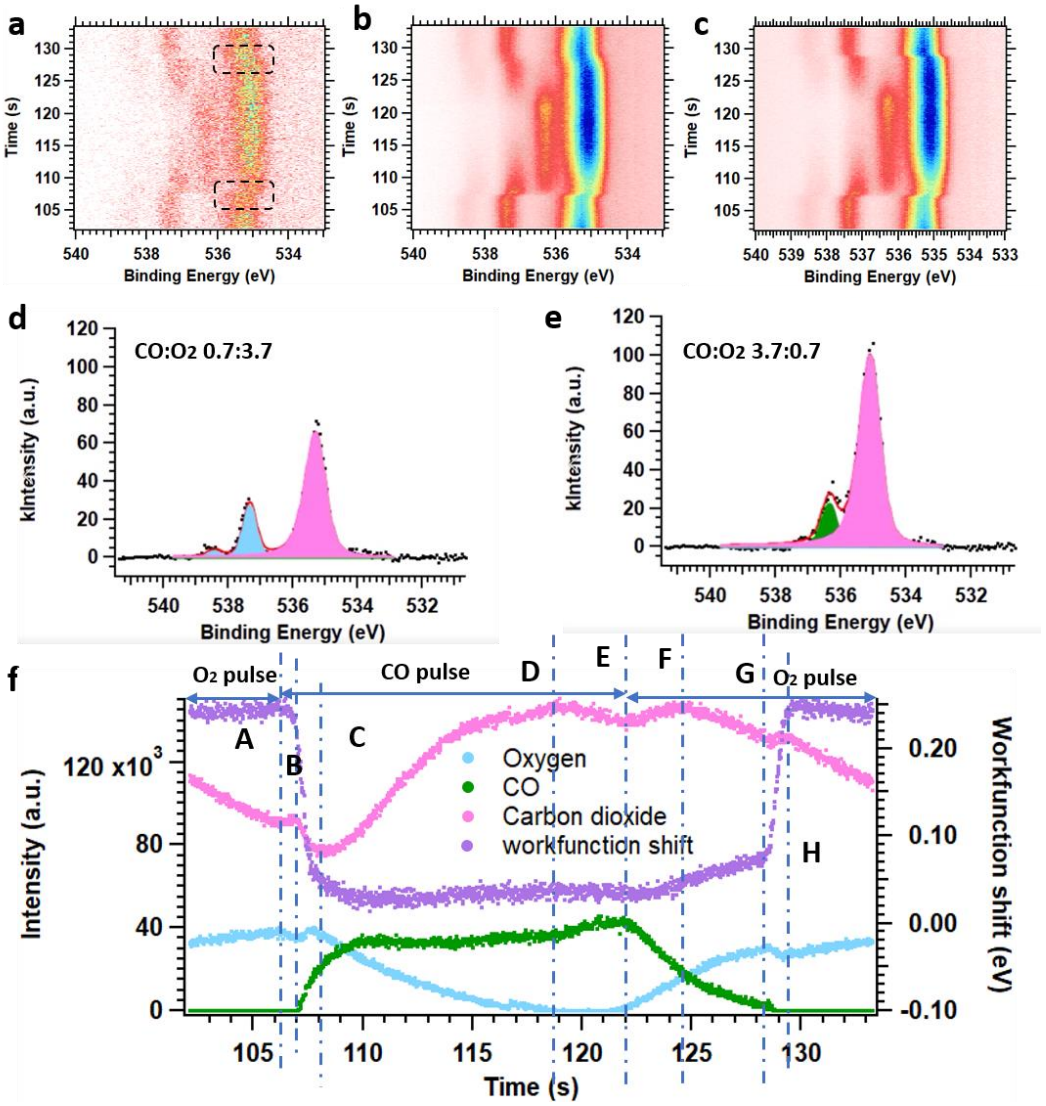


*Figure 16 The gas phase measurement of O1s spectra with time resolution a) before, and after event-averaging of 90 pulses with b) one stamp, and c) two stamps. The single spectrum extracted from the time-resolved spectra during d) $O_2$ rich pulse, and e) CO rich pulse. f) The $O_2$, CO and $CO_2$ components intensity with time evolution, and the binding energy shift.*

In the following section all measurements were recorded with the sample retracted by 1 mm. The result of this is that we selectively probe gas phase molecules in front of the sample surface while core- and secondary electrons originating from the solid sample surface do not reach the electron analyzer. Figure 16 shows the gas phase measurement of the O 1s spectra measured with 52.6 Hz before (a), and after event averaging of 90 pulses with one (b) and two (c) stamp signals, respectively. In total each image plot contains 1640 O 1s spectra. Single spectra extracted from the time-resolved spectra in panel c and acquired in the $O_2$ rich pulse (t=105.0 s), and CO rich pulse (t=117.7 s) are shown in panel d and e, respectively. Panel f shows the time evolution of the $O_2$, CO and $CO_2$ component intensities together

with the common workfunction shift observed by changing apparent binding energy shifts of the gas phase components.

Comparing Figure 16a with Figure 14a showing O 1s gas phase and surface spectra, respectively, it becomes clear that the signal-to-noise ratio is improved substantially for the gas phase spectra.

Similar to the O 1s spectra from surface measurement which also probed the gas phase molecules Figure 16d shows three components, of which the two blue components with the highest binding energy at 537.4 and 538.5 eV are assigned to $O_2$ doublet, while the pink component at 535.3 eV is attributed to $CO_2$. In Figure 16e under the CO rich environment, the $O_2$ gas phase signal disappears. Instead CO is observed with a binding energy of 536.3 eV. Due to the surface work function shift of 0.2 eV after the surface structrue change, the binding energy of $CO_2$ signal shifts to 535.1 eV.

Discussing the data shown in Figure 16f the intensity of $O_2$ component slightly increases in the beginning until t=106 s (line A) indicating an accumulation of the $O_2$ in the gas phase. In the meantime the $CO_2$ production from the Pd surface and the filament decreased. The system is in the CO mass transfer limit, consistent with the O 1s surface measurement.

Just after t=106 s (line A) until t=106.8 s (line B), the $CO_2$ signal increases slightly while the $O_2$ signal decrease slightly. This was not observed in surface O 1s data. indicating the gas pulse changes at this point. This is due to the injection of CO in the cell facilitating the reaction. The sample work function from line A to B remains constant revealing the unchanged oxidized surface structure. As no gas phase CO is observed the reaction must be mass transfer limited by CO.

From line B to line C (t=108.2 s), the work function shift shows a rapid change, together with a reduced $CO_2$ production and an increased $O_2$ signal, revealing a surface structure change. In the meantime, the CO signal is also observed to increase. The Pd surface changes to CO covered structure and the reaction is suppressed, which might also be the reason for the temporary increment of $O_2$.

As the CO signal increases, the Pd surface should turn inactive. However, from line C to line D (t=119 s) the $CO_2$ production increases and more $O_2$ is consumed. We explain this by increased conversion on the hot Pt filament. As the Pd surface becomes inactive the exothermic heat of the reaction is lost and the Pt filament starts to heat more to maintain the same temperature. After reaching line D, the $O_2$ signal becomes 0, followed by a decreased $CO_2$ production which we did not observe in surface measurements. Now the reaction is mass transfer limited by $O_2$.

At line E (t = 122 s), the CO signal starts decreasing while the $O_2$ signal increases, signaling the shift of the gas composition. A slight change of the work function is observed from line E to F (124.5 s). This is clear evidence that the surface structure changes. We propose that some CO-vacancies are formed facilitating minor $O_2$ adsorption on the surface. The $CO_2$ production goes down from line F to G (128.5 s), which is in a contradiction with the surface measurement result, but giving a more reasonable result since the filament reaction should be suppressed due to the reducing CO in the cell.

A rapid change of the work function starts from line G, resulting from a total removal of CO on the surface replaced by the oxide. At line H (t = 129.4 s), the surface is fully oxidized. It is then followed by a suppressed reaction on the filament due to the CO mass transfer limit.

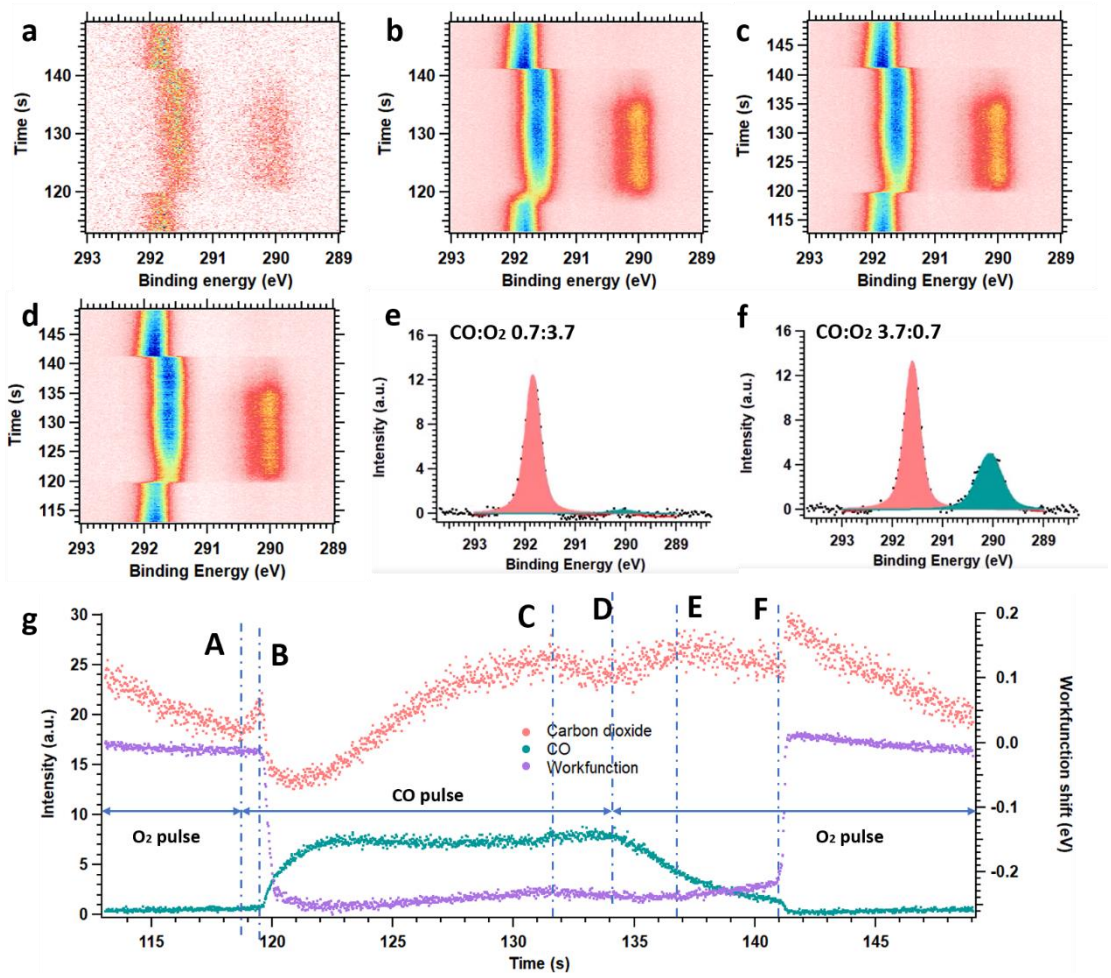


*Figure 17 Time resolved C 1s gas phase measurement a) before, and after event-averaging of 90 pulses with b) one stamp, c) two stamps, and d) after background removal, and intensity normalization. The single spectrum extracted from the time-resolved spectra during e) $O_2$ rich pulse, and f) CO rich pulse. g) The $CO_2$ and CO components intensity and the binding energy shift with time evolution.*

The C 1s gas phase measurement is conducted in the same way as the O 1s gas phase experiments. The image plot shown in Figure 17a shows 1726 spectra, with a time duration of 36 s, containing one full CO pulse in the middle. The measurement frequency was 48 Hz. With the same methods done for the measurements above, the image plot was event-averaged over 91 pulses by using one stamp signal (Figure 17b), and two stamp signals (Figure 17c) to increase the signal-to-noise ratio. Figure 17d shows the image plot after background removal and intensity normalization. Figure 17e and f show two single spectra extracted from $O_2$ rich gas composition (t=115.7 s) and CO rich gas composition (t=130.2 s), respectively. Only a pink component is observed at 291.8 eV in the $O_2$ rich gas composition (see Figure 17e), assigned to $CO_2$. Due to the surface structure change, the $CO_2$ component shifts to 291.6 eV in CO rich gas composition in Figure 17f, in addition with a CO component (green) observed at 290.1 eV in this gas composition.

Figure 17g shows the time evolution of the CO, $CO_2$ component intensity and workfunction shift. Inspection of panel g shows that the $CO_2$ production initially decreases due to a mass transfer limit of the

CO. At line A (t = 118.7 s) a sharp increase is observed and 1 second later the workfunction starts shifting (line B).

Now the surface oxide is removed and CO adsorbs. As it is discussed in the previous work[25], CO has higher affinity to metallic Pd surface than Pd oxide, and the surface is quickly turned inactive. Therefore, the $CO_2$ production decreases significantly. As the exothermic heat of the surface reaction is lost, the filament needs to heat more, and its temperature increase leading increased $CO_2$ production on the filament. Now the filament is the main reaction site again and remains active during the entire CO pulse period although it is suppressed due to mass transfer limit of $O_2$ at line C (t=131.7). The reactivity returns at line D (t=134.1 s) when the gas composition shifts back to $O_2$ rich period. The surface structure remains covered by CO until line E (t=137.8 s) where small increase of the surface workfunction is observed. Now some oxygen occupies CO-vacancies on the surface and the reaction is now following the Langmuir–Hinshelwood mechanism with a very low reaction rate.

A new observation in line F (t=141 s) shows an abrupt increment of $CO_2$, and a sharp work function shift, during which the CO in the gas phase is removed. The observation of the $CO_2$ increment was missing in the other measurement above due to the noise of signals, and the interruption by the filament. This observation gives direct evidence that the surface shifts from being CO covered to oxidize covered with a significant improved reaction rate. The high signal-to-noise ratio acquired in C 1s allows us the observe the surface phase transition from the CO covered metallic phase to an oxidized surface. The following variation of the intensities are same as what we discussed above.

### 4.3.3. Statistical analysis of CO signal in the gas phase

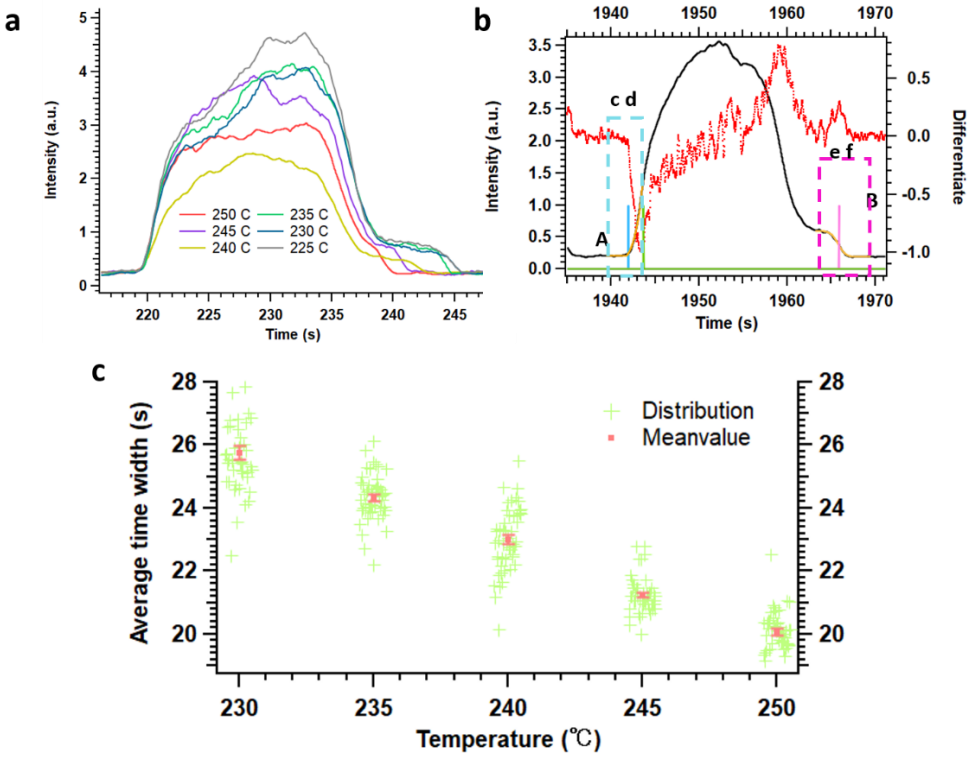


*Figure 18 a) Single CO pulse signal integrals under sample temperatures from 225 to 250 ℃. b) A single CO signal (dark curve) and its differentiate (red curve). The marked regions of onset (cd), and plateau (ef) are curve fitted with two functions and the A, and B points are the defined starting point and ending point of the signal determined by the fitting function, respectively. c) The single signal width distribution and the calculated mean value of with error bar showing the corresponding standard deviation of the mean values under different temperatures.*

The analysis of event-averaged image plots above showed that the $CO_2$ production starts increasing at the end of the CO signal before the surface was fully oxidized. In the meantime, the CO pressure decreases. Interestingly, the CO pressure reach a lower plateau level just before the surface is oxidized.

In this section, we analyze the CO plateau level as measured in the C 1s gas phase image plots as function of sample temperature. By integrating the signal along the time axis, the CO signal as function of time was obtained. Figure 18a shows the CO signal integrals with the time length of 30 seconds under a series of temperatures from 225 to 250 ℃ with identical pulses setting of all the data set (15 s of CO rich pulse plus 15 s of $O_2$ rich pulse with CO to $O_2$ ratio of 3.7: 0.7 and 0.7:3.7, respectively) and with the onset of all the curves aligned. At the beginning, the CO signal increase rapidly. It continues to increase with a decreasing growth rate until it reaches saturation. Subsequently, the CO signal decreases and eventually becomes zero when the surface becomes oxidized. The CO plateau lasting for ~ 5 s is easy to observed in the figure between 225 and 235 s.

From the comparison of the measurement performed at different temperatures, it is observed that the time length of the pulse, which starts from the CO rich pulse injection to the oxide development on the surface, is temperature dependent. With a lower temperature, a longer plateau is obtained.

Here, the CO plateau reveals a stable level of CO in the cell. That is, the CO is either not participating in the reaction or it is reacting with a constant rate. Correlating the gas phase O 1s and C 1s time evolution analysis in Figure 16f and Figure 17g, the CO plateau meets with the decrease of $CO_2$ production due to the MTL on the filament and the presence of CO on the surface. It reveals that no active reaction is taking place in this regime. We declare it as a "silent regime". After a few seconds of the plateau, an abrupt drop to zero of CO occurs together with the removal of CO on the surface and development of oxide. Therefore, we propose the "silent regime" is the preparation for the exchange between the CO adsorption to oxide development. The temperature dependence of the plateau length indicates that it might be related to the activate energy required to overcome the energy barriers to lift off the CO from the surface in replacement by the oxygen.

To study if this time length always is the same, we quantitively analyzed the width of the signal integrals from ~ 100000 spectra obtained from ~ 50 pulses for each temperature. Two edges of the CO signal are defined to be the onset point of the curve shown as the point A in Figure 18b, and the midpoint of the step shown as the point B. Two fitting functions were used at the two regions to determine the edge points. For the onset of the curve, we fitted the curve in the region cd shown in the Figure 18c with a constant line followed by an exponential function.

$$f(x) = w[0] \ \ (x \leq w[1])$$

$$f(x) = w[0] - e^{\frac{w[1]-w[2]}{w[3]}} + e^{\frac{x-w[2]}{w[3]}} \ \ (x \geq w[1])$$

The step region ef of the signal curve were fitted with error function

$$f(x) = B + A \cdot \mathrm{erf}\left(\frac{x-P}{W}\right)$$

Where P is the turning point and defined as the end edge of the curve, and B is the y value of the turning point. Once both edges of the integral curves are found, the width of each curve is determined. Figure 18c shows the mean value (red cross) of the CO component integral from all pulses under different temperatures, which were given to be 25.745, 24.342, 23.01, 21.235, and 20.066 s from 230 to 250 °C. The temperature of 225 °C is too low to activate the surface, and no oxide was developed. Thus, we here only analyzed the data from 230 to 250 °C. The distribution of the CO integral curve width under different operation temperatures is shown as green dots. It is obvious, that the width of the CO integral in general decreases as temperature increases, which aligns the results from a single pulse in Figure 18a. A linear trend line is shown for the width-temperature plot the Figure 18c. The standard deviation of the mean value under each temperature were given as the error bar which is given by

$$\sigma_{mean} = \frac{\sqrt{\Sigma(y_i - \bar{y})^2}}{n}$$

Whereas $y_i$ is the value of each point, $\bar{y}$ is the mean value, and n is the total number of the points. From 230 to 250 °C, the standard deviation of the mean value were given to be 0.094, 0.078, 0.138, 0.098, and 0.210, which reveals a high consistence between each CO integral curves under the same temperature. A comparably high value of standard deviation from the data under 230 °C might because of not fully oxidized surface from some pulses due to the low operation temperature, which gives a higher diversity of the CO integral curve shape.

I would like to highlight the analysis in Figure 18c, is a real quantitative analysis of many pulses. This is very uncommon in the APXPS literature. In almost all previous studies one surface transition is studied. Clearly our work here demonstrates that one should be careful with such an approach as the individual data points for each temperature scatter considerably. In contrast, our statistical analysis of more than 50 pulses for each temperature clearly reveal the temperature dependence of the CO signal time length in a convincing way.

# 5. Conclusion

In this thesis, gas composition oscillation combined with APXPS was used to study CO oxidation on the Pd(100) surface and how the surface structure and catalyst activity changes in response to the oscillations. The cyclic gas pulsing combined with event-averaging by image recognition was for the first time applied at the SPECIES beamline at the MAX IV laboratory. By analyzing time-resolved C 1s, O 1s from both gas phase and surface, and Pd $3d_{5/2}$ from surface, we reached the following conclusions:

1. By event-averaging, the signal-to-noise ratio of the time resolved spectra was highly improved and peak decomposition and phase transition became possible to study. By recording the time evolution of the surface components and local gas composition, the dynamics of surface structure change, and the surface reactivity during the gas pulse oscillation was followed.
2. By the time evolution analysis of the different components we draw the following conclusions:
    a. Even with improved time-resolution compared to previous works[9, 11, 16] the fast phase transition is still impossible to resolve due to the limited time resolution of ~17 ms (60 Hz).
    b. The time resolved spectra after event-averaging gas phase spectra are in general better than the signal-to-noise ratio in surface measurements. Therefore, a sharper phase transition is observed in event-averaged gas phase image plots.
    c. Dual reactions from both Pd surface and Pt filament took place in parallel in the SPECIES setup. Unfortunately, the filament reaction was the major source of $CO_2$ production in the cell. However, even with the huge interruption from the filament, it still was possible to study the surface reaction.
    d. The removal of CO from the surface and the oxide development take place in parallel and the process is very abrupt under the observation by APXPS. In the meantime of the CO replenished by oxide, a rapid increase of $CO_2$ production is observed. The surface turns to active before fully oxidized.
3. Considering the different pulse length and varying instrument frequency during measurement, a statistic analysis of CO gas phase signal was performed for the first time. A clear temperature dependence of the time the surface spend in the CO poisoned state was found.

# 6. Further outlook

During the thesis work, I identified barriers for event-averaging method I used:

1. Event-averaging has its limitation. It cannot fully solve the low time resolution of XPS. We still cannot demonstrate if there is faster intermediate process during the reaction, and the reactivity of CO covered Pd surface and oxide surface have not successfully demonstrated. To improve the frequency of the instrument is the only fundamental way to resolve the fast process such as phase transition, segregation processes.
2. The interruption from Pt filament during the entire data analysis cannot be ignored. It is not ideal to use another active catalyst materials as heater when studying the catalyst surface chemistry study. It would be helpful in the further a carbon based heated can be installed in this APXPS instrument.

# Reference

(1) Kalz, K. F.; Kraehnert, R.; Dvoyashkin, M.; Dittmeyer, R.; Glaser, R.; Krewer, U.; Reuter, K.; Grunwaldt, J. D. Future Challenges in Heterogeneous Catalysis: Understanding Catalysts under Dynamic Reaction Conditions. *ChemCatChem* **2017,** *9* (1), 17-29, DOI: 10.1002/cctc.201600996.
(2) Toyoshima, R.; Kondoh, H. In-situ observations of catalytic surface reactions with soft x-rays under working conditions. *J Phys Condens Matter* **2015,** *27* (8), 083003, DOI: 10.1088/0953-8984/27/8/083003.
(3) Roiaz, M.; Pramhaas, V.; Li, X.; Rameshan, C.; Rupprechter, G. Atmospheric pressure reaction cell for operando sum frequency generation spectroscopy of ultrahigh vacuum grown model catalysts. *Rev. Sci. Instrum.* **2018,** *89* (4), 045104, DOI: 10.1063/1.5021641.
(4) Hartfelder, U.; Singh, J.; Haase, J.; Nachtegaal, M.; Grolimund, D.; van Bokhoven, J. A. Detecting and utilizing minority phases in heterogeneous catalysis. *Sci Rep* **2016,** *6*, 37597, DOI: 10.1038/srep37597.
(5) Ryczkowski, J. IR spectroscopy in catalysis. *Catal. Today* **2001,** *68* (4), 263-381.
(6) Kostelník, P.; Seriani, N.; Kresse, G.; Mikkelsen, A.; Lundgren, E.; Blum, V.; Šikola, T.; Varga, P.; Schmid, M. The surface oxide: A LEED, DFT and STM study. *Surf. Sci.* **2007,** *601* (6), 1574-1581, DOI: 10.1016/j.susc.2007.01.026.
(7) Miller, B. K.; Crozier, P. A. Linking Changes in Reaction Kinetics and Atomic-Level Surface Structures on a Supported Ru Catalyst for CO Oxidation. *ACS Catalysis* **2021,** *11* (3), 1456-1463, DOI: 10.1021/acscatal.0c03789.
(8) van Spronsen, M. A.; Frenken, J. W. M.; Groot, I. M. N. Observing the oxidation of platinum. *Nat Commun* **2017,** *8* (1), 429, DOI: 10.1038/s41467-017-00643-z.
(9) Lundgren, E.; Zhang, C.; Merte, L. R.; Shipilin, M.; Blomberg, S.; Hejral, U.; Zhou, J.; Zetterberg, J.; Gustafson, J. Novel in Situ Techniques for Studies of Model Catalysts. *Acc. Chem. Res.* **2017,** *50* (9), 2326-2333, DOI: 10.1021/acs.accounts.7b00281.
(10) Zhu, S.; Scardamaglia, M.; Kundsen, J.; Sankari, R.; Tarawneh, H.; Temperton, R.; Pickworth, L.; Cavalca, F.; Wang, C.; Tissot, H.; Weissenrieder, J.; Hagman, B.; Gustafson, J.; Kaya, S.; Lindgren, F.; Kallquist, I.; Maibach, J.; Hahlin, M.; Boix, V.; Gallo, T.; Rehman, F.; D'Acunto, G.; Schnadt, J.; Shavorskiy, A. HIPPIE: a new platform for ambient-pressure X-ray photoelectron spectroscopy at the MAX IV Laboratory. *J Synchrotron Radiat* **2021,** *28* (Pt 2), 624-636, DOI: 10.1107/S160057752100103X.
(11) Blomberg, S.; Hoffmann, M. J.; Gustafson, J.; Martin, N. M.; Fernandes, V. R.; Borg, A.; Liu, Z.; Chang, R.; Matera, S.; Reuter, K.; Lundgren, E. In situ x-ray photoelectron spectroscopy of model catalysts: at the edge of the gap. *Phys. Rev. Lett.* **2013,** *110* (11), 117601, DOI: 10.1103/PhysRevLett.110.117601.
(12) Knudsen, J.; Gallo, T.; Boix, V.; Stromsheim, M. D.; D'Acunto, G.; Goodwin, C.; Wallander, H.; Zhu, S.; Soldemo, M.; Lomker, P.; Cavalca, F.; Scardamaglia, M.; Degerman, D.; Nilsson, A.; Amann, P.; Shavorskiy, A.; Schnadt, J. Stroboscopic operando spectroscopy of the dynamics in heterogeneous catalysis by event-averaging. *Nat Commun* **2021,** *12* (1), 6117, DOI: 10.1038/s41467-021-26372-y.
(13) Park, R. L.; Madden Jr, H. H. Annealing changes on the (100) surface of palladium and their effect on CO adsorption. *Surf. Sci.* **1968,** *11* (2), 188-202.
(14) Hendriksen, B. L. M.; Bobaru, S. C.; Frenken, J. W. M. Oscillatory CO oxidation on Pd(100)

studied with in situ scanning tunneling microscopy. *Surf. Sci.* **2004,** *552* (1-3), 229-242, DOI: 10.1016/j.susc.2004.01.025.
(15) Zhou, J.; Blomberg, S.; Gustafson, J.; Lundgren, E.; Zetterberg, J. Visualization of Gas Distribution in a Model AP-XPS Reactor by PLIF: CO Oxidation over a Pd(100) Catalyst. *Catalysts* **2017,** *7* (12), 29, DOI: 10.3390/catal7010029.
(16) Fernandes, V. R.; Bossche, M. V. d.; Knudsen, J.; Farstad, M. H.; Gustafson, J.; Venvik, H. J.; Grönbeck, H.; Borg, A. Reversed Hysteresis during CO Oxidation over Pd75Ag25(100). *ACS Catalysis* **2016,** *6* (7), 4154-4161, DOI: 10.1021/acscatal.6b00658.
(17) Piednoir, A.; Languille, M. A.; Piccolo, L.; Valcarcel, A.; Cadete Santos. Aires, F. J.; Bertolini, J. C. Pd(111) versus Pd–Au(111) in carbon monoxide oxidation under elevated pressures. *Catal. Lett.* **2007,** *114* (1-2), 110-114, DOI: 10.1007/s10562-007-9047-3.
(18) Chen, M.; Wang, X. V.; Zhang, L.; Tang, Z.; Wan, H. Active surfaces for CO oxidation on palladium in the hyperactive state. *Langmuir* **2010,** *26* (23), 18113-8, DOI: 10.1021/la103140w.
(19) van Rijn, R.; Balmes, O.; Resta, A.; Wermeille, D.; Westerstrom, R.; Gustafson, J.; Felici, R.; Lundgren, E.; Frenken, J. W. Surface structure and reactivity of Pd(100) during CO oxidation near ambient pressures. *Phys. Chem. Chem. Phys.* **2011,** *13* (29), 13167-71, DOI: 10.1039/c1cp20989b.
(20) Hellman, A.; Resta, A.; Martin, N. M.; Gustafson, J.; Trinchero, A.; Carlsson, P. A.; Balmes, O.; Felici, R.; van Rijn, R.; Frenken, J. W.; Andersen, J. N.; Lundgren, E.; Gronbeck, H. The Active Phase of Palladium during Methane Oxidation. *J Phys Chem Lett* **2012,** *3* (6), 678-82, DOI: 10.1021/jz300069s.
(21) Toyoshima, R.; Yoshida, M.; Monya, Y.; Kousa, Y.; Suzuki, K.; Abe, H.; Mun, B. S.; Mase, K.; Amemiya, K.; Kondoh, H. In Situ Ambient Pressure XPS Study of CO Oxidation Reaction on Pd(111) Surfaces. *The Journal of Physical Chemistry C* **2012,** *116* (35), 18691-18697, DOI: 10.1021/jp301636u.
(22) Toyoshima, R.; Yoshida, M.; Monya, Y.; Suzuki, K.; Mun, B. S.; Amemiya, K.; Mase, K.; Kondoh, H. Active Surface Oxygen for Catalytic CO Oxidation on Pd(100) Proceeding under Near Ambient Pressure Conditions. *J Phys Chem Lett* **2012,** *3* (21), 3182-7, DOI: 10.1021/jz301404n.
(23) Lorenzi, J. M.; Matera, S.; Reuter, K. Synergistic Inhibition of Oxide Formation in Oxidation Catalysis: A First-Principles Kinetic Monte Carlo Study of NO + CO Oxidation at Pd(100). *ACS Catalysis* **2016,** *6* (8), 5191-5197, DOI: 10.1021/acscatal.6b01344.
(24) Rogal, J.; Reuter, K.; Scheffler, M. First-principles statistical mechanics study of the stability of a subnanometer thin surface oxide in reactive environments: CO oxidation at Pd(100). *Phys. Rev. Lett.* **2007,** *98* (4), 046101, DOI: 10.1103/PhysRevLett.98.046101.
(25) Hendriksen, B. L.; Ackermann, M. D.; van Rijn, R.; Stoltz, D.; Popa, I.; Balmes, O.; Resta, A.; Wermeille, D.; Felici, R.; Ferrer, S.; Frenken, J. W. The role of steps in surface catalysis and reaction oscillations. *Nat Chem* **2010,** *2* (9), 730-4, DOI: 10.1038/nchem.728.
(26) Gao, F.; Wang, Y.; Cai, Y.; Goodman, D. CO oxidation on Pt-group metals from ultrahigh vacuum to near atmospheric pressures. 2. Palladium and platinum. *The Journal of Physical Chemistry C* **2009,** *113* (1), 174-181.
(27) Schnadt, J.; Knudsen, J.; Andersen, J. N.; Siegbahn, H.; Pietzsch, A.; Hennies, F.; Johansson, N.; Martensson, N.; Ohrwall, G.; Bahr, S.; Mahl, S.; Schaff, O. The new ambient-pressure X-ray photoelectron spectroscopy instrument at MAX-lab. *J Synchrotron Radiat* **2012,** *19* (Pt 5), 701-4, DOI: 10.1107/S0909049512032700.
(28) Urpelainen, S.; Sathe, C.; Grizolli, W.; Agaker, M.; Head, A. R.; Andersson, M.; Huang, S. W.;

Jensen, B. N.; Wallen, E.; Tarawneh, H.; Sankari, R.; Nyholm, R.; Lindberg, M.; Sjoblom, P.; Johansson, N.; Reinecke, B. N.; Arman, M. A.; Merte, L. R.; Knudsen, J.; Schnadt, J.; Andersen, J. N.; Hennies, F. The SPECIES beamline at the MAX IV Laboratory: a facility for soft X-ray RIXS and APXPS. *J Synchrotron Radiat* **2017,** *24* (Pt 1), 344-353, DOI: 10.1107/S1600577516019056.
(29) Schmitz-Antoniak, C. X-ray absorption spectroscopy on magnetic nanoscale systems for modern applications. *Rep. Prog. Phys.* **2015,** *78* (6), 062501, DOI: 10.1088/0034-4885/78/6/062501.
(30) Greczynski, G.; Hultman, L. X-ray photoelectron spectroscopy: Towards reliable binding energy referencing. *Prog. Mater Sci.* **2020,** *107*, 100591, DOI: 10.1016/j.pmatsci.2019.100591.
(31) Miller, A.; Powell, C. J.; Gelius, U.; Anderson, C. Energy calibration of X-ray photoelectron spectrometers. Part III: Location of the zero point on the binding-energy scale. *Surface and Interface Analysis: An International Journal devoted to the development and application of techniques for the analysis of surfaces, interfaces and thin films* **1998,** *26* (8), 606-614.
(32) Watts, J. F. X-ray photoelectron spectroscopy. *Surface science techniques* **1994,** *45* (5).
(33) Jain, V.; Biesinger, M. C.; Linford, M. R. The Gaussian-Lorentzian Sum, Product, and Convolution (Voigt) functions in the context of peak fitting X-ray photoelectron spectroscopy (XPS) narrow scans. *Appl. Surf. Sci.* **2018,** *447*, 548-553, DOI: 10.1016/j.apsusc.2018.03.190.
(34) Todorova, M.; Lundgren, E.; Blum, V.; Mikkelsen, A.; Gray, S.; Gustafson, J.; Borg, M.; Rogal, J.; Reuter, K.; Andersen, J. N.; Scheffler, M. The Pd()–R27°-O surface oxide revisited. *Surf. Sci.* **2003,** *541* (1-3), 101-112, DOI: 10.1016/s0039-6028(03)00873-2.
(35) Behm, R. J.; Christmann, K.; Ertl, G.; Van Hove, M. A. Adsorption of CO on Pd(100). *The Journal of Chemical Physics* **1980,** *73* (6), 2984-2995, DOI: 10.1063/1.440430.
(36) Rogal, J.; Reuter, K.; Scheffler, M. COoxidation atPd(100): A first-principles constrained thermodynamics study. *Physical Review B* **2007,** *75* (20), DOI: 10.1103/PhysRevB.75.205433.